Bachelor's Thesis

AFM-Imaging of Moiré Superpotentials in Twisted Bilayer Graphene on Soft Polymer Stamps

AFM-Abbildungen von Moiré Superpotentialen in gedrehtem zweilagigen Graphen auf weichen Polymer Stempeln

Department of Physics
Ludwig-Maximilians-Universität München

Quentin Fuchs

Munich, September 2nd, 2024

Submitted in partial fulfillment of the requirements for the degree of B. Sc.
Supervised by Prof. Dr. Dmitri Efetov and Dr. Martin Lee

Abstract

This thesis addresses the critical need for reliable moiré imaging in the study of twisted bilayer graphene (tBG) devices, which are challenging to reproduce due to the complexities of stacking and twisting graphene monolayers. Leveraging the atomic force microscopy - torsional force microscopy (AFM-TFM) mode, where the cantilever operates at its torsional resonance, we mapped changes in amplitude or phase induced by dynamic friction to visualize the moiré pattern. This method, unlike other modes, does not require a conductive substrate, allowing for rapid feedback during fabrication, even when placed on soft polymers.

This work extends previous studies by exploring a broader range of parameters and incorporating non-optimal images to facilitate discussion and guide replication. It provides a detailed Standard Operating Procedure (SOP) and a comprehensive overview of the AFM setup, theoretical background, and fabrication techniques. Our findings confirm that TFM, with the provided SOP, is effective in imaging moirés close to the MATBG condition, enabling the identification of bubbles, wrinkles, strain, and edges across multiple devices. The procedure is efficient, requiring only 30 minutes to obtain the first moiré image and 1-2 hours for full device mapping.

Ultimately, the SOP developed in this thesis is poised to enhance the fabrication process within the community, contributing to advancements in the 2D materials field.

Contents

Chapter 1

Introduction

The discovery and understanding of new materials have historically driven technological advancements, revolutionized industries and reshaped society. For instance, the in-depth knowledge of semiconducting materials, particularly silicon, has been instrumental in the development of critical technologies such as computer chips, batteries, and sensors. As we approach the limits of Moore's Law [1], which predicts the doubling of transistors on a microchip approximately every two years, the quest for new materials to enhance chip performance becomes imperative [2]. After the discovery of graphene in 2004 [3], which consists of a single layer of carbon atoms, various other two-dimensional (2D) materials, have garnered significant attention due to their remarkable electronic properties. These properties arise from the unique quantum effects that emerge from their reduced dimensionality [3]. Recent developments suggest that applications in computer chips and sensors may soon be realized [4, 5]. Significant improvements in performance and efficiency are expected, making the continued exploration and development of these materials highly promising [6].

The combination of different 2D materials through stacking and twisting has led to the creation of Van-der-Waals (vdW) heterostructures [7]. They have opened new routes for engineering novel materials with unique properties [8, 9, 10]. The interlayer coupling is decisive for the presence and nature of charge redistribution and correlated phenomena, resulting in emergent properties not present in the individual layers. There are different methods for tuning coupling between layers, with twisting being a particularly interesting example. The resultant properties are highly dependent on the twist angle, denoted as θ, and can coexist in the proximity of different carrier densities within the same material system [11]. When materials with similar lattice structures are twisted relative to each other, they form an interference pattern known as a moiré superlattice. Twisted bilayer graphene (tBG) is especially noteworthy in this context, as it exhibits a range of fascinating phases. Close to a specific twist angle, known as the "magic angle" of $\theta = 1.05^\circ$ [12], the electronic band structure develops flat bands. As a result, this magic angle twisted bilayer graphene (MATBG) features remarkable phases of matter, including superconductivity [8], correlated insulators [9], and various other quantum phases [10], depending on the band filling.

Despite the high potential of tBG and its fascinating properties, many studies highlight a significant challenge: the poor controllability of θ during the fabrication process [13]. This lack of precision leads to difficulties in reproducing the desired properties reliably across different samples. However, recent advances in the fabrication process have shown that anchoring the edges of the graphene sheets on a hexagonal boron nitride (hBN) support - a technique known as clamping — can significantly enhance the yield in terms of desired devices [14]. To further improve the fabrication process, a rapid and reliable technique for visualizing the moiré pattern was developed by Pendhakar et al. in [15]. This method allows a straightforward observation of the moiré pattern, even while the tBG is still on a polymer stamp, facilitating better control of tBG devices. The adaptation and implementation of this technique within the field form the central focus of this thesis. By integrating this approach, we aim to achieve a more consistent and precise fabrication of tBG.

By imaging the moiré pattern using Atomic Force Microscopy (AFM) and measuring the periodicity of the superlattice, the twist angle can be accurately calculated [16]. This method allows for quick identification of devices, that are close to the MATBG condition, enabling researchers to select optimal candidates for further experiments before finalizing device fabrication. In addition to characterizing entire devices, this technique can pinpoint promising areas that are free from strain and bubbles. Furthermore, this method has the potential to image the moiré superlattice in a variety of materials, extending its applicability beyond graphene.

This straightforward approach utilizes Torsional Force Microscopy (TFM) to measure samples in air and at room temperature. Unlike other AFM modes [17, 18, 19], TFM does not require any preprocessing, such as the use of conductive substrates nor conductive coating of cantilevers. By providing quick feedback, this technique enhances the efficiency and precision of fabricating and analyzing tBG. These devices are typically used in transport measurements, which are crucial for our understanding of the properties of 2D materials.

In Chapter 2 we discuss the theoretical background of mono-, bilayer, and twisted bilayer graphene with emphasis on the bandstructure and the emergent electronic properties. Furthermore, the analytical solutions of the resonances for a beam-shaped cantilever are provided. In Chapter 3.1 the basic operation modes of AFM are examined with a focus on TFM, in Chap. 3.2 the fabrication process for tBG and the post processing of the obtained images in Chap. 3.3 is provided. The obtained images and influence of different parameters are discussed in the results in Chap. 4. An instruction-like documentation of each step, required for successful imaging, is provided in the standard operating procedure in the Appendix A.

Chapter 2

Theoretical background

2.1 Graphene basics

Carbon atoms can form various structures, such as diamond and graphite, each with unique properties. Graphene is a form, consisting of a single layer of carbon atoms arranged in a hexagonal lattice. Before its discovery in 2004, the stability of two-dimensional (2D) materials like graphene was debated, as thermodynamic fluctuations were thought to prevent such materials from existing as flat surfaces [20]. Although similar structures of different topologies, such as carbon nanotubes (1D) or fullerene (0D [21] had been discovered, isolating a 2D atomic layer was challenging. Creating atomically thin films required epitaxial growth techniques [22]. This method has a significant drawback because the graphene layer is strongly bonded to the substrate and doesn't show π-bands, which are found to be crucial for the electronic properties of graphene [23]. In 2004, Andre Geim and Konstantin Novoselov successfully isolated graphene using mechanical exfoliation and studied the electronic properties[3]. This method, which is still widely used, demonstrated the feasibility of obtaining stable, and clean graphene monolayers and paved the way for its extensive study and application.

This Chapter discusses the crystal structure and then continues by analyzing the band structure of mono- and bilayer graphene using tight-binding calculations. Following that, the properties of twisted bilayer graphene will be presented, with a specific focus on the moiré superlattice and the magic angle condition.

2.1.1 Single layer graphene

The following section on bonding in graphene is based on the book in [24]. Each carbon atom has four valence electrons available for bonding, located in the 2s and 2p orbitals. These electrons undergo hybridization, which is the mixing of different orbitals to form new hybrid orbitals that are energetically favorable for binding. Specifically, graphene exhibits sp^2 hybridization, illustrated in Fig. 2.1, with a trigonal planar geometry. In this configuration, the three hybrid orbitals form strong covalent σ-bonds with neighboring carbon atoms, creating a stable hexagonal lattice. The fourth valence electron, residing

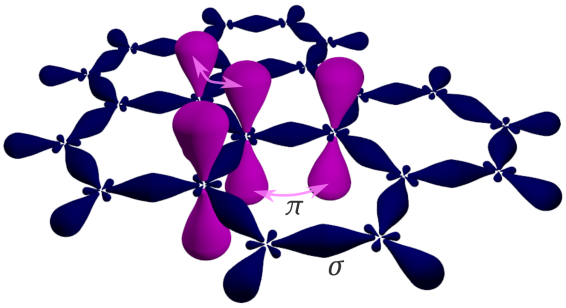

Figure 2.1: *Through sp^2 hybridization strong σ-bonds are formed, leading to a hexagonal lattice (dark blue). Weaker π-bonds are formed between the remaining p_z orbitals at each atom (pink). Adapted from [26].*

in the unhybridized p_z orbital, forms a weaker π-bonds through the lateral overlap with p_z orbitals of neighboring atoms. The π-bonding, occurring out of the plane, is crucial for the remarkable electrical conductivity of graphene. The delocalized nature of these π electrons gives rise to high electron mobility, facilitating electron transport [25, 24]. In later tight-binding calculations in this thesis, only the electrons in the p_z orbitals are considered since the electrons in the σ-bonds are strongly localized [25].

For the tight binding calculations presented in this section, we will define a crystallographic basis as shown in Fig. 2.2. Here the lattice vectors a_i, b_i (i=1,2) are defined as

$$\vec{a}_1 = \frac{a}{2} \cdot (3, \sqrt{3}), \tag{2.1}$$
$$\vec{a}_2 = \frac{a}{2} \cdot (3, -\sqrt{3}),$$
$$\vec{b}_1 = \frac{2\pi}{3a} \cdot (1, \sqrt{3}), \tag{2.2}$$
$$\vec{b}_2 = \frac{2\pi}{3a} \cdot (1, -\sqrt{3}).$$

The nearest neighbors are defined as δ_i (i=1,2,3)

$$\vec{\delta}_1 = \frac{a}{2} \cdot (1, \sqrt{3}), \tag{2.3}$$
$$\vec{\delta}_2 = \frac{a}{2} \cdot (1, -\sqrt{3}),$$
$$\vec{\delta}_3 = -a \cdot (1, 0).$$

and the Dirac points K and K' as

$$K = \frac{2\pi}{3a}(1, \sqrt{3}), \tag{2.4}$$
$$K' = \frac{2\pi}{3a}(1, \sqrt{3}).$$

Due to crystallographic symmetry, the hexagonal lattice is considered as two interpenetrating triangular lattices, referred to as A and B sublattices. The graphene unit cell comprises two inequivalent atoms (A and B). We will return to the importance of the two Dirac points in the discussion of the band structure of graphene.

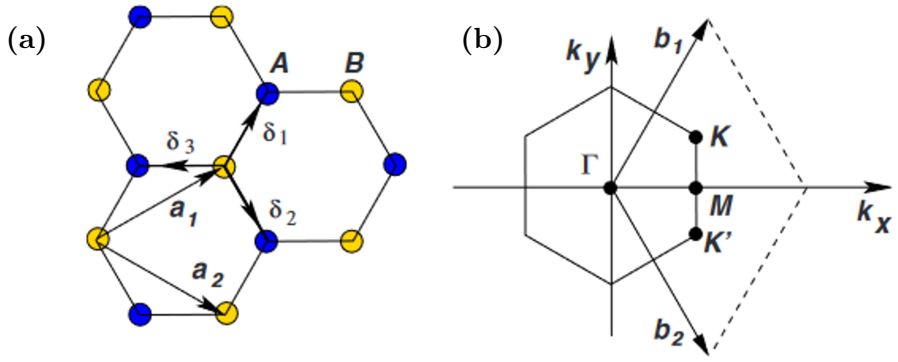

Figure 2.2: *(a) Shows real space graphene hexagonal lattice, with the lattice vectors of a primitive unit cell are denoted as* $\mathbf{a}_i$ *(i=1,2) and the nearest neighbors vectors as* $\boldsymbol{\delta}_i$ *(i=1,2,3). The blue and yellow dots show crystallographic inequivalent atoms A and B in the sublattice. (b) The reciprocal lattice with 1st BZ, reciprocal lattice vectors* $\mathbf{b}_i$ *(i=1,2) and Dirac points at the edge of the BZ, named K and K'. Adapted from Fig. 2 of [27].*

The theoretical work on the bandstructure of graphene was first conducted by Wallace in 1947 [25]. Additionally, we will base the following calculations on a comprehensive report and book [27, 24].

Graphene's electronic band structure can be effectively modeled using the tight-binding approach, which is well-suited for complex crystal structures like graphene. This model closely matches experimental data [28] and provides an intuitive, analytically solvable understanding of graphene's electronic behavior, particularly near the Dirac points [27]. For improved accuracy, second-order hopping terms can be added, or more comprehensive methods like Density Functional Theory (DFT) can be used, offering a deeper insight into graphene's electronic properties [24]. Bloch's theorem ensures that the evaluation of the bandstructure can be limited to the 1st BZ without loss of generality [29]. The Hamiltonian in natural units, only considering nearest neighbor hopping, which is equivalent to hopping between different sublattices A and B is

$$H = -t \sum_{\langle i,j \rangle, \sigma} \left(a^{\dagger}_{i,\sigma} b_{j,\sigma} + \text{H.c.}, \right) \tag{2.5}$$

Where $a^{\dagger}_{\sigma,j}$, $a_{\sigma,j}$ are creation/annihilation operators of electrons respectively, on sublattice A at site $\mathbf{R}_j$ with spin $\sigma =\uparrow,\downarrow$. The definition of $b_{\sigma,j}$ in sublattice B is equivalent. H.c. denotes the Hermitian conjugate, that is needed to ensure real eigenvalues. $t \approx 2.8eV$ is the nearest neighbor hopping energy. The next-nearest neighbor hopping term is small compared to t and can be neglected [30]. Transforming the Hamiltonian into reciprocal space and diagonalizing the 2x2 matrix we can find the following eigenvalues or dispersion relation [25]:

$$E_{\pm}(\mathbf{k}) = \pm t\sqrt{3 + f(\mathbf{k})} \text{ with } f(\mathbf{k}) = 2\cos\left(\sqrt{3}k_y a\right) + 4\cos\left(\frac{\sqrt{3}}{2}k_y a\right)\cos\left(\frac{3}{2}k_x a\right), \quad (2.6)$$

Here a is the lattice constant and k is the electron momentum, and +,- denote the conduction and valence band of the π-electrons respectively. The spectrum is symmetric around 0 energy, with electron-hole symmetry and touching bands at the Dirac points leading to graphene being a zero-gap semiconductor. First order expanding the dispersion relation around $\mathbf{K}$ vector with $\mathbf{k} = \mathbf{K} + \mathbf{q}$ and $|\mathbf{q}| \ll |\mathbf{K}|$ leads to a linear dispersion, as derived in [25]

$$E_{\pm}(\mathbf{q}) = \pm v_{\mathrm{F}}|\mathbf{q}|, \quad (2.7)$$

Here $v_{\mathrm{F}} = 1 \times 10^6\,\mathrm{m/s}$ is the Fermi velocity. Note that this velocity does not depend on neither the mass nor the energy, and the dispersion relation exhibits a linear behavior. Figure 2.3 displays the band structure where the Dirac points are shown in the inset. The linearity and shape at those points lead to the term "Dirac cones". The effective Hamiltonian of the expansion in Eq. 2.1.1 is equivalent to the 2D Dirac Hamiltonian. This equivalence arises from the Dirac equation in quantum electrodynamics (QED) by setting the rest mass to zero. Consequently, electrons near the Dirac points in graphene behave as massless Dirac fermions, exhibiting relativistic behavior despite being non-relativistic particles [24].

The effective Hamiltonian also exhibits similarities to the spinor Hamiltonian and introduces a concept known as valley pseudospin. This additional degree of freedom, akin to a quantum number, arises from the presence of two distinct valleys in the Brillouin zone (K, K'). Since intervalley hopping is typically negligible [27], graphene's band structure is inherently fourfold degenerate when considering both valley and spin degrees of freedom. However, this degeneracy can be lifted by breaking certain symmetries, such as time-reversal or inversion symmetry. As we will see later, examples of such symmetry-breaking scenarios include twisted bilayer graphene and hBN. They lead to modifications in the electronic properties and band structure of the material [24]. Introducing a next-nearest neighbor hopping term would also already break the electron-hole symmetry [27].

After introducing the lattice vectors and the tight binding Hamiltonian and its solution for monolayer graphene we will discuss in the following chapter the nature of bilayer graphene in a similar fashion.

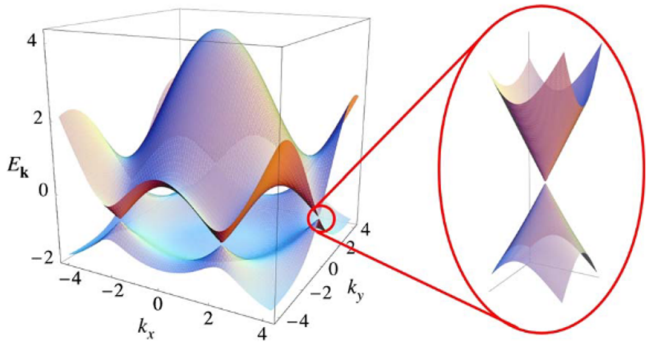

Figure 2.3: *The band structure of graphene with an enlarged view of the Dirac points. The energy is given in units of the hopping term t. Points with such a linear dispersion and distinctive shape are referred as "Dirac cones". Adapted from Fig. 3 of [27].*

2.1.2 Bilayer graphene

Bilayer graphene is created by stacking two monolayers of graphene on top of each other, resulting in a material with emergent electronic properties. The two graphene layers are weakly bound by vdW forces, which are much weaker than the covalent bonds within each monolayer [27]. This weak interaction allows for the relative sliding and rotational movements between the layers. In bilayer graphene, the most common stacking configuration is the AB (or Bernal) stacking, where the second layer is shifted relative to the first. This leads to distinct electronic characteristics, such as a tunable band gap and an altered electronic dispersion compared to single-layer graphene. These properties make bilayer graphene a versatile material for a range of applications in electronics and material science.

When introducing interlayer hopping terms into the Hamiltonian of BG (Eq. 2.1.1), a strong similarity to the tBG becomes apparent.

$$\begin{aligned}\hat{H} = &- t \sum_{\langle i,j\rangle,\sigma} \left(a^{\dagger}_{(1,i,\sigma)} b_{(1,j,\sigma)} + \text{H.c.} \right) \\ &- t \sum_{\langle i,j\rangle,\sigma} \left(a^{\dagger}_{(2,i,\sigma)} b_{(2,j,\sigma)} + \text{H.c.} \right) \\ &- t_{\perp} \sum_{i,\sigma} \left(a^{\dagger}_{(2,i,\sigma)} b_{(1,i,\sigma)} + \text{H.c.} \right)\end{aligned} \tag{2.8}$$

We use the same notation as in 2.1.1, with 1,2 in subscript for the different layers. The first two terms describe the individual layers and the third term is an interlayer mixing term. AB stacking exhibits a high hopping term of $t_{\perp} \approx 0.4eV$ for hopping from A_2 to B_1 (A_2 - B_1), while hopping A_1 - B_2 can be neglected [27]. Solving the eigenvalue problem and expanding around K, in a similar manner to obtain Eq. 2.1.1, gives rise to the dispersion relation

$$E_{\pm}(\mathbf{k}) = V^2 + v_F^2 k^2 + \frac{t_\perp^2}{2} \pm \sqrt{4V^2 v_F^2 k^2 + t^2 v_F^2 k^2 + \frac{t_\perp^4}{4}}, \tag{2.9}$$

Where V denotes the difference in electrochemical potential between the two layers. For $V = 0$, the dispersion is quadratic with two bands touching at $E = 0$ and two additional bands starting at $t_\perp$. this leads to the bilayer graphene showing metallic behavior [27]. This result, seen in Fig. 2.4 (a), is quite different from the bandstructure in a single layer, showed in Fig. 2.3. When applying an electrochemical bias, the shifted difference in electrochemical potential V opens up a bandgap, seen in Fig. 2.4 (b), because a nonzero electrochemical potential $V \neq 0$ breaks the inversion symmetry. This is a striking result for technological application because the ability to tune the bandgap by applying a bias makes bilayer graphene a promising candidate for a new generation of transistors [27].

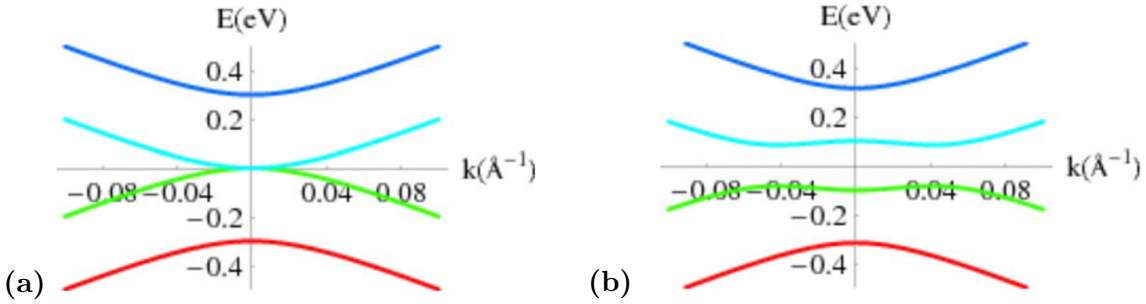

Figure 2.4: *The bandstructure of bilayer graphene when only considering interlayer A_2 - B_1 hopping. (a) At $V = 0$, parabolic bands touch at $E = 0$, with two additional bands starting at $E = t_\perp \approx 0.4eV$ (b) At $V \neq 0$, a bandgap opens up corresponding to the shift in the difference of electrochemical potential between two layers. Adapted from Figs. 10-11 in [27].*

2.1.3 Twisted bilayer graphene

In the AB stacking configuration, seen in Fig. 2.5 (b), the second layer is shifted relative to the first layer so that its B atoms (B_2, indicating the second layer) are positioned at the center of the hexagons formed by the first layer. Meanwhile, its A atoms (A_2) are aligned directly above the B atoms of the bottom layer (B_1). AA stacking is energetically the most costly configuration and SP (saddle point) appears as domain walls between AB and BA regions.

As mentioned in the chapter 1, the moiré pattern is an interference of the potential of two layers of 2D materials, introduced by a lattice mismatch because of rotational misalignment. This new periodic potential, referred as superpotential, with a real-space periodicity approximately 50 times larger than the lattice constant of single-layer graphene at $\theta \approx 1.1°$, resulting in a much smaller BZ. This superpotential directly influences the electronic band structure, leading to novel states and phenomena.

The moiré pattern generates distinct stacking regions AA, AB/BA and SP, visible in AFM images. In the AB stacking configuration, seen in Fig. 2.5 (b), the second layer

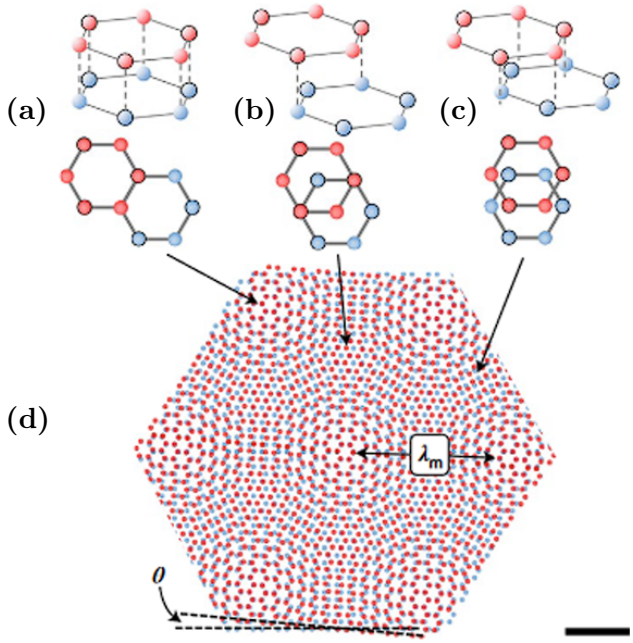

Figure 2.5: *Different stacking configurations (a) AA, (b) AB, (c) domain walls (saddle points) SP, appear simultaneously in tBG and form the moiré superpotential. (d) Representative moiré lattice with a twist angle θ and periodicity λ (later denoted as d). Adapted from Fig. 1 of [17].*

is shifted relative to the first layer so that its B atoms (B_2, indicating the second layer) are positioned at the center of the hexagons formed by the first layer. Meanwhile, its A atoms (A_2) are aligned directly above the B atoms of the bottom layer (B_1). AA stacking is energetically the most costly configuration and SP (saddle point) appears as domain walls between AB and BA regions. The density of states depends on the configuration with the electron density being strongly concentrated on the AA regions, whereas mostly deprecated in the AB, BA regions [9].

When introducing a twist angle, the resulting superpotential causes the number of atoms per unit cell to increase significantly, leading to computational challenges in tight-binding calculations. To manage this complexity, the so-called continuum model is often employed, especially near critical points like the Dirac points [31, 12]. Similar to Eq. 2.1.2 the Hamiltonian consists of two intralayer and one interlayer hopping term. The interlayer hopping can be described as a tunneling term with an amplitude between π-orbitals as a smooth function $t(r)$. The intralayer Hamiltonian of one layer which is rotated by θ with respect to a fixed coordinate system is given by [12]

$$H_{\mathrm{k}}(\theta) = -v_{\mathrm{F}} k \begin{bmatrix} 0 & e^{i(\theta_{\mathrm{k}}-\theta)} \\ e^{-i(\theta_{\mathrm{k}}-\theta)} & 0 \end{bmatrix}, \tag{2.10}$$

with θ_{k} as the momentum orientation with respect to the x-axis. The matrix element $T^{AB}_{k\mathbf{p}'}$ of the tunneling Hamiltonian H_{T} describes the tunneling of an electron placed in sublattice A in one layer with momentum $\boldsymbol{p}'$. This electron hops to a state in the other layer in sublattice B with momentum $\boldsymbol{k}$

$$T^{AB}_{k\mathbf{p}'} = \langle \Psi^{(1)}_{kA} | H_T | \Psi^{(2)}_{\mathbf{p}'B} \rangle \tag{2.11}$$

with $\Psi^{(i)}_{kj}$, i = (1, 2) and j = (A, B) describing the tight binding wavefunction of the two different layers i with sublattice j. Using these wavefunctions explicitly yields a useful form of the matrix element. In this model, hopping is assumed to be local and periodic, such that Bloch's theorem can still be applied [12]. The obtained matrix must be solved numerically but exhibits much less computational effort compared with tight binding models [12]. The obtained bandstructure by the continuum model is shown in Fig. 2.6 for different twist angles θ. The two Dirac points K and K‘ are highlighted by the vertical gray lines in the middle and the right of each graph. As we will discuss below, the lowest energy bands become flat bands near zero Fermi energy at certain angles, here $\theta = 1.05$, which induces quantum phenomena.

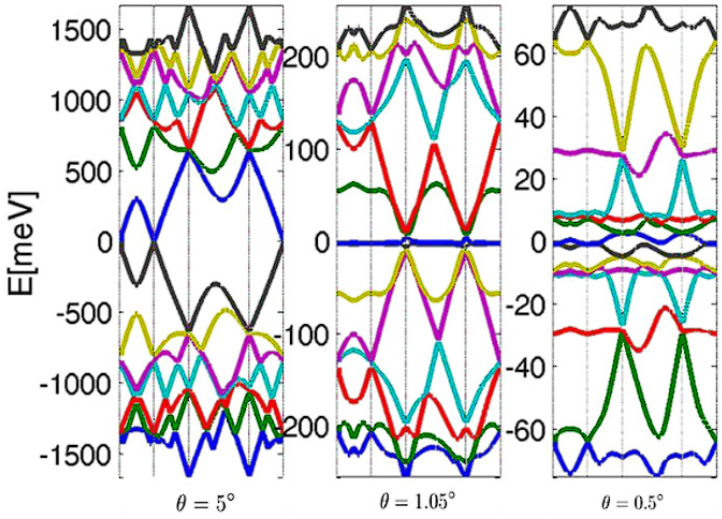

Figure 2.6: *Shows the bandstructure of tBG obtained by the continuum model for different twist angles θ. At $\theta = 1.05$ the lowest energy bands become flat near zero Fermi energy, inducing quantum phenomena. Two Dirac points K and K‘ are highlighted by the vertical gray lines in the middle and the right of each graph. Adapted from Fig. 3 of [12].*

We now discuss some key effects of tBG more qualitatively. For twisted materials with a small twist angle ($\theta < 2°$) the bands start hybridizing. As seen in Fig. 2.7 (a) the two Dirac points K^1 and K^2 (K'^1 and K'^2) are moving closer together as θ decreases. Interlayer hybridization happens between Dirac cones within each valley (with the same value of valley pseudospin), while interlayer processes are strongly suppressed [9]. A key finding of Ref. [12] is that the bandstructure of tBG can be described to first order by a single parameter α [12] and the renormalized Fermi velocity v_F

$$\alpha = \frac{w}{\hbar v_{\mathrm{F}} k_\theta}, \qquad v_{\mathrm{F}} = v_0 \frac{1 - 3\alpha^2}{1 + \alpha^2} \tag{2.12}$$

Here w is the hopping energy between two layers and k_θ is the moiré wavevector. It shows the ratio between the magnitude of hybridization (w) and the kinetic energy of the electrons. The Fermi velocity is renormalized (v_0 from single layer graphene) and vanishes multiple times at different small angles, named magic angles, of which the smallest is at $\theta \approx 1.1°$. At this angle, the band structure undergoes remarkable changes: the bands become degenerate flat bands near the zero Fermi energy. The electrons within these flat bands, have very low kinetic energies, leading to their localization. For an illustration of the hybridization of Dirac cones see Fig. 2.7. At half-filling, where exactly half of the available states are filled with electrons, the system exhibits insulating behavior [9]. However, by changing the carrier density through electrostatic doping this insulating state can be shifted into an unconventional superconducting phase. By doing so, the symmetry of the system is broken, allowing for the emergence of superconductivity [11].

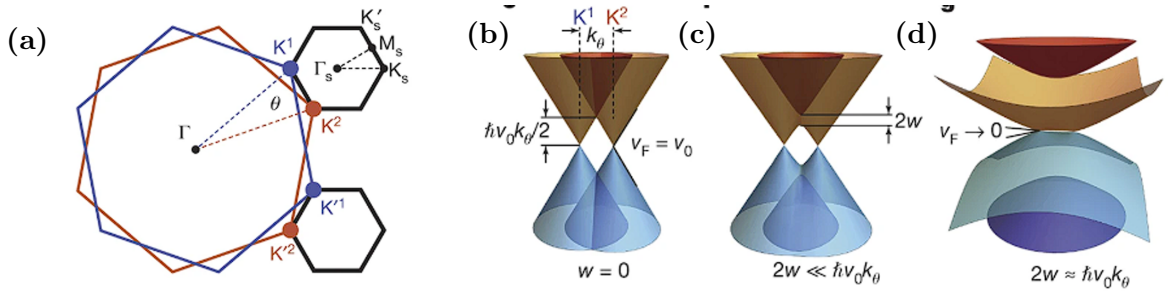

Figure 2.7: *(a) The BZ of two graphene layers (red and blue) twisted by θ. As θ decreases, the two Dirac points K^1 and K^2 (K'^1 and K'^2) move closer together and hybridize. The black hexagonal is the mini-BZ of the moiré unit cell. (b-c) The hybridization of Dirac cones at different interlayer hopping energies, leading to the opening of a bandgap. (d) At the magic angle condition the bands flatten, leading to the renormalized Fermi velocity $v = 0$. Adapted from Fig. 1 of [9].*

After presenting the band structures and highlighting the differences of mono-, bilayer, and MATBG we emphasize the importance of moiré imaging. To further explore the fascinating quantum phases and validate relativistic quantum dynamics (Dirac Fermions), induced by linear dispersion relations near the Dirac points [24], we need to achieve a high yield of desired devices in the vicinity of the MATBG regime. The yield can be further improved by providing feedback through moiré imaging. Considering the potentially high rewards of technological applications mentioned in the Introduction (Chap. 1), it is essential to have a reliable imaging procedure during device fabrication.

2.2 Torsional resonances of a beam-shaped cantilever

In section 3.1, which discusses the working principle of AFM, the focus shifts to the motivation behind selecting the specific mode of TR-Dynamic Friction Microscopy (TR-DFM or TFM) and its measuring routine for friction induced by moiré superlattices. This method is based on torsional resonances. To lay the groundwork, an overview of the

analytical solution of different resonance modes is provided in the following.

The analytical solution for a beam-shaped cantilever is based on the Bernoulli-Euler beam theory. The differential equation of the motion of the vibration is given in Ref. [32]

$$EI\frac{\partial^4 v(x,t)}{\partial x^4} + \rho A\frac{\partial^2 v(x,t)}{\partial t^2} = 0 \tag{2.13}$$

Here E is the Young's modulus, ρ the density of the material, I the moment of inertia of the cross-sectional area A, and $v(x,t)$ is the displacement, depending on time and axial location x. This theory applies to the limiting case of small displacement scenarios involving a vertical load on the cantilever [33]. In the case of a cantilever beam, the following boundary condition applies for a free end at $x = L$ [32]

$$EI\left.\frac{\partial^2 v(x,t)}{\partial x^2}\right|_{x=L} = 0, \quad \text{and} \quad EI\left.\frac{\partial^3 v(x,t)}{\partial x^3}\right|_{x=L} = 0, \tag{2.14}$$

and a clamped end at $x = 0$

$$v(x=0,t) = 0, \quad \text{and} \quad EI\left.\frac{\partial v(x,t)}{\partial x}\right|_{x=0} = 0, \tag{2.15}$$

Using a separation ansatz for $v(x,t)$ and the geometry of the cantilever, one obtains the solution for resonant frequency as provided in the Bruker Application note on TR mode in Ref. [33]. The lateral bending and torsional modes can overlap, therefore we provide the analytical solution for both. We consider a cantilever with thickness t and width w. The resonance frequency for lateral bending is

$$f_{\text{lat bending}} = \frac{\alpha_i}{2\pi L}\sqrt{\frac{EI}{\rho A}} = \frac{\alpha_i}{2\pi L}\sqrt{\frac{Ew^2}{12\rho}}, \quad \text{with} \quad I = \frac{w\cdot t^3}{12}, \quad \text{and} \quad A = w\cdot t. \tag{2.16}$$

Here I and A are the moment of inertia and cross-sectional area of a rectangular cantilever, and $\alpha_i = 1.875$ is the first analytical solution of the characteristic equation of a free-fixed beam. The torsional modes can be calculated similarly but with different moments of inertia and boundary conditions. For the torsional modes, stress and strain are non-uniform and we need to introduce a correction factor ξ. When the thickness is much smaller than the width ($t \ll w$) we can further simplify the solution for the resonant frequency. The torsional resonance frequency is found to be

$$f_{\text{torsion}} = \frac{1}{4L}\cdot\sqrt{\frac{\xi G}{\rho I_p}} \approx \frac{t}{2Lw}\cdot\sqrt{\frac{G}{\rho}} \quad \text{with,} \tag{2.17}$$

$$\xi = \frac{1}{3}w\cdot h_t^3\left(1 - 0.632\frac{h_t}{w}\right), \quad \text{and} \quad I_{\text{p}} = \frac{t^3 w}{12} + \frac{w^3 t}{12}, \tag{2.18}$$

Here $G = \frac{E}{2(1+\nu)}$ is the shear modulus of the material, where ν is the Poisson's ratio and I_p is the polar moment of inertia. The used cantilever thickness in our experiments, results in the torsional mode always being positioned above the lateral bending mode with a space of $\sim$ 300 kHz [33].

For a more detailed analysis, particularly involving the cantilever's tip, Finite Element Method (FEM) simulations are required, since the complex shape cannot be solved analytically. Using the most suitable boundary conditions is crucial as well, since this affects the obtained solutions of the differential equation substantially. Including the tip disrupts the cantilever's symmetry, resulting in a well-defined and sharply peaked torsional resonance mode [33]. Chapter 3.1.4 discusses that there is no way to distinguish between lateral bending and torsional resonance modes with the experimental setup of an AFM. From a practical perspective, the actual torsional resonances are obtained by sweeping over a certain interval (Appendix A).

Chapter 3

Methods

3.1 Atomic force microscopy

Having previously highlighted the significance of moiré imaging in guiding the stacking process, we will now delve deeper into the underlying motivation and continue by providing an overview of the fundamentals of AFM, with particular emphasis on the specific mode used in this work: TFM. Specific instructions for obtaining high-resolution moiré images are provided in the standard operating procedure (SOP) in the Appendix A.

3.1.1 The motivation of moiré imaging

In Ref. [17] (2020), McGilly et al. accurately described the challenges in existing high-resolution techniques for visualizing moiré superlattices, such as transmission electron microscopy (TEM) and scanning tunneling microscopy (STM). They often require ultra-high vacuum conditions, low temperatures, complex setups, or specialized sample preparation. These demanding requirements make these methods impractical for routine use. Other approaches, like near-field optics and transport with multiple contacts, lack the required resolution to observe moiré periods of interest. For the MATBG condition, a periodicity of $\sim$10 nm is usually obtained. This highlights the urgent need for a simpler and more accessible method for characterizing moiré superlattices [17]. Pendhakar et al. demonstrated in Ref. [15] in 2024, that using the so-called TFM mode, allows imaging on an insulating polymer stamp, providing significantly faster feedback during fabrication with subnanometer resolution, that reaches atomic scale.

Due to its large significance in improving the challenging fabrication process of MATBG and its capabilities of characterizing electronic properties like the work function, moiré imaging has emerged as a major research focus in recent years. Currently, the most common modes have been piezo force microscopy (PFM) [17], [19] and Kelvin probe force microscopy (KPFM) [18]. Conductive AFM (C-AFM) has been demonstrated to achieve atomic resolution in Ref. [34]. All three modes were generally considered to require a conductive tip and sample. For a complete overview of the moiré imaging capabilities of different modes, we refer to table S1. in [35].

3.1.2 The AFM basics

Following the invention of Scanning Probe Microscopy (SPM) in 1982 [36], several related techniques have been developed, with AFM being a relevant form. AFM, invented in 1986 by G. Binnig, C. Gerber, and C. Quate, measures the forces on the atomic scale between a surface and a sharp probe tip [37]. It detects cantilever motion by using a photodiode to track the deflection of a laser beam reflecting on the cantilever. This enables the production of high-resolution topographical images. Depending on the mode, the cantilever is driven at different kinds of resonances, providing either vertical bending or torsional oscillation. It utilizes various feedback loops and provides different outputs, like amplitude, phase, or height sensor data, sometimes with a physical meaning like the work function. An important advantage of AFM is that it can be applied to conductive, semiconductive, and insulating materials [38]. The technique employs a raster scan pattern, systematically moving across the surface in multiple lines until the defined scan area is fully mapped. Here we provide a basic overview of the most important modes for moiré imaging:

1. Contact mode: In contact mode, the AFM tip remains in contact with the surface while maintaining a fixed force. The cantilever's deflection is continuously monitored by the photodiode, allowing the collection of topographical information on the sample. The feedback loop adjusts to keep the deflection at a setpoint, ensuring the applied force remains constant throughout the scan [38].

2. Tapping mode: In tapping mode, the cantilever oscillates vertically near its resonance frequency, allowing the tip to tap the sample surface briefly. As the tip encounters different surface heights, the amplitude changes. These changes are fed back to the piezo, such that the resulting amplitude is kept constant with varying drive amplitude. The change in amplitude is mapped to provide an image of the sample topography. These variations provide detailed surface topography information while minimizing sample damage [39].

3. Kelvin probe force microscopy (KPFM): KPFM involves applying an AC bias between the AFM tip and the sample, generating an electrostatic force between the two, that varies with the local surface potential. By measuring the amplitude and phase of the resulting cantilever deflection, KPFM can map the surface potential and work function distribution with nanoscale precision [40].

4. Piezo force microscopy (PFM): In PFM, an AC bias is applied between the tip and the sample, inducing periodic deformations in the sample. The amplitude and phase of these deformations, detected through the torsion or deflection of the cantilever, provide local information about the sample's electromechanical properties, such as piezoelectricity [17, 18].

As shown in Fig. 3.1 (a), an AFM operates with a basic setup that includes a laser, cantilever, and photodiode. The laser beam first passes through a collimator and lens, focusing it onto a reflectively coated cantilever. The cantilever reflects the laser beam, which then travels through another lens and is directed by two mirrors, of which one is adjustable, towards the photodiode. The photodiode detects any deflection of the laser

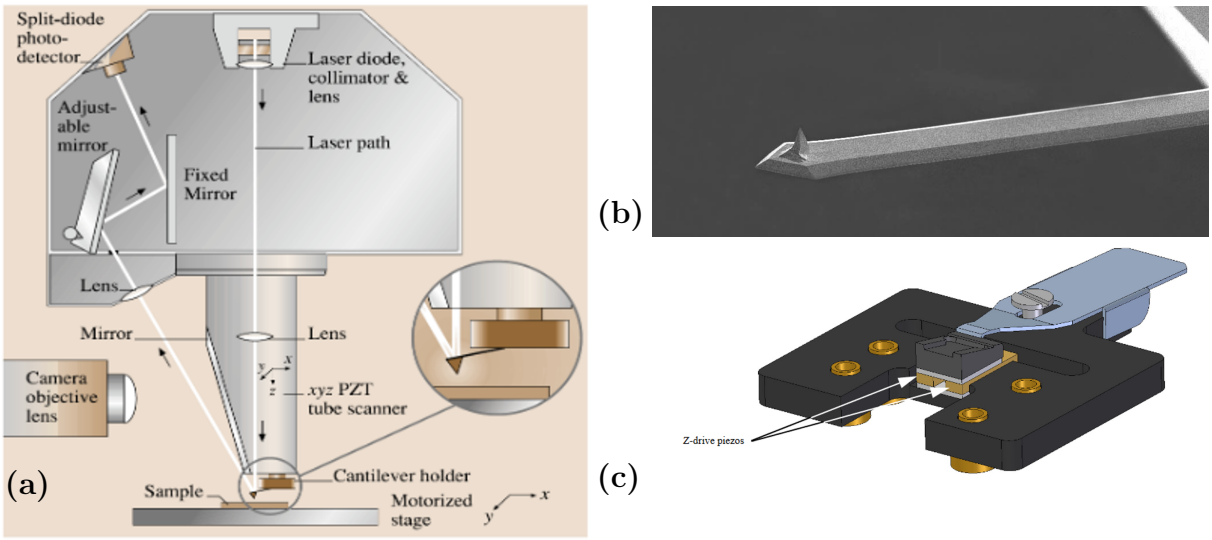

Figure 3.1: *(a) Basic AFM setup: A laser is focused onto a reflectively coated cantilever, which deflects the beam onto a photodiode via lenses and adjustable mirrors. A high-resolution camera aids in sample navigation and laser alignment. (b) TEM image of the beam-shaped cantilever with the tip mounted on the free end (type HQ: NSC18 Al Bs). (c) Probe holder with two piezos, for torsional drive and 4 contacts to the scan head (type: Bruker DTRCH). (a) Adapted from Fig. 3.2 of [41], (b) from MikroMasch [*`https://www.spmtips.com/afm-tip-hq-nsc18-al-bs`*], (c) from Fig. 3e of [33].*

beam with high accuracy. From this, the cantilever's movement can be determined. Additionally, a high-resolution camera is employed for navigating the sample surface and aligning the laser beam with the cantilever.

The AFM probe consists of a sharp tip (typical tip radius is $r \leq 20\,\text{nm}$), that interacts with the surface, and a rectangular cantilever or beam that measures micrometers (see Fig. 3.1 (b)). The cantilever exhibits mechanical properties such as bending and torsional resonance, akin to a beam. The probe holder features four contacts between the scan head and the two piezoelectric actuators that are driven out of phase to achieve torsional motion (see Fig. 3.1 (c)).

3.1.3 Discovery of TFM for moiré imaging

During an attempt to replicate PFM measurements by McGilly et al. [17], where an AC bias is applied to the tip while the sample is grounded, an unexpected discovery was made by Pendharkar et al. [15]. In their setup, a probe holder, similar to the holder used in this work, contained three traces connected to the torsional piezo and one dead-end trace, usually used in PFM for applying an AC bias to the tip. When no effective ground nor tip bias was applied, a high-resolution moiré image can still be obtained, which cannot originate from the piezoelectric response of the sample. They attempted to apply a bias near the torsional resonance frequency to the tip through the inactive trace on the tip holder. The torsional piezos were driven via electronic crosstalk, reaching levels of $\sim$ 2-2.5%, which is considered reasonable by Bruker. In Fig. 3.2, the response to direct

and crosstalk mediated resonant driving of the piezos in the TR mode is compared. The latter exhibits $\sim 2\%$ less response than the former. This finding raises questions about the accuracy of previous PFM studies, particularly those applying bias near the torsional resonance. Instead of using crosstalk-driven piezos, directly driving the system in TR mode offers several advantages, including precise control over the torsional piezos and access to specialized software tools available in this mode [15, 35].

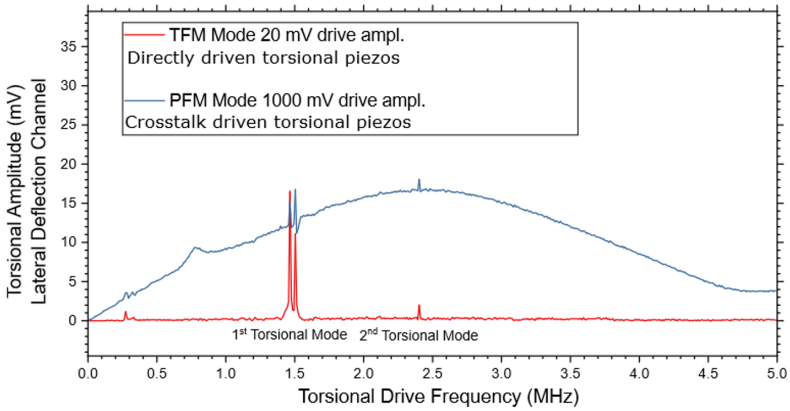

Figure 3.2: *A comparison is shown of resonance response when directly driving the piezos in TR mode versus unintentional driving via crosstalk. This exhibits $\sim$ 2% lower response in the latter. The torsional modes' position heavily depends on the cantilever's geometry, therefore the spectrum is shaped differently compared to the one we obtained. Adapted from Fig. S1 of of [35]*

3.1.4 Measuring dynamic friction in the TR mode

The term TFM, named by the authors [15], refers to TR - dynamic friction (TR-DFM) by Bruker itself [42], describing the actual measurand. TR-DFM provides a significant advantage over other dynamic friction modes. Unlike conventional contact mode techniques, such as lateral force microscopy (LFM), TR-DFM images are only marginally affected by surface topography, offering more accurate characterization of frictional properties [42]. Additionally, TR-DFM are generally insensitive to the scanning direction of the tip [42], which is a notable improvement over techniques like PFM, where the sample must be manually rotated by 90° [17].

The process, of obtaining TR-DFM images, involves mapping the spatial variations in the torsional resonances of the cantilever. This operation is carried out in two parallel loops: a closed feedback loop and an open loop. The two loops, as well as the key components of TFM, are schematically shown in Fig. 3.3. The closed loop (denoted as purple) operates similarly to traditional contact modes like PFM, where it tracks the topography by maintaining a constant vertical loading force between the tip and the sample. This ensures constant contact during scanning, allowing the cantilever to accurately follow the surface profile. The open loop (denoted as green), on the other hand, is responsible for exciting the torsional resonance of the cantilever and mapping the mechanical response. The TR amplitude or phase of the cantilever's torsional oscillation, which are sensitive

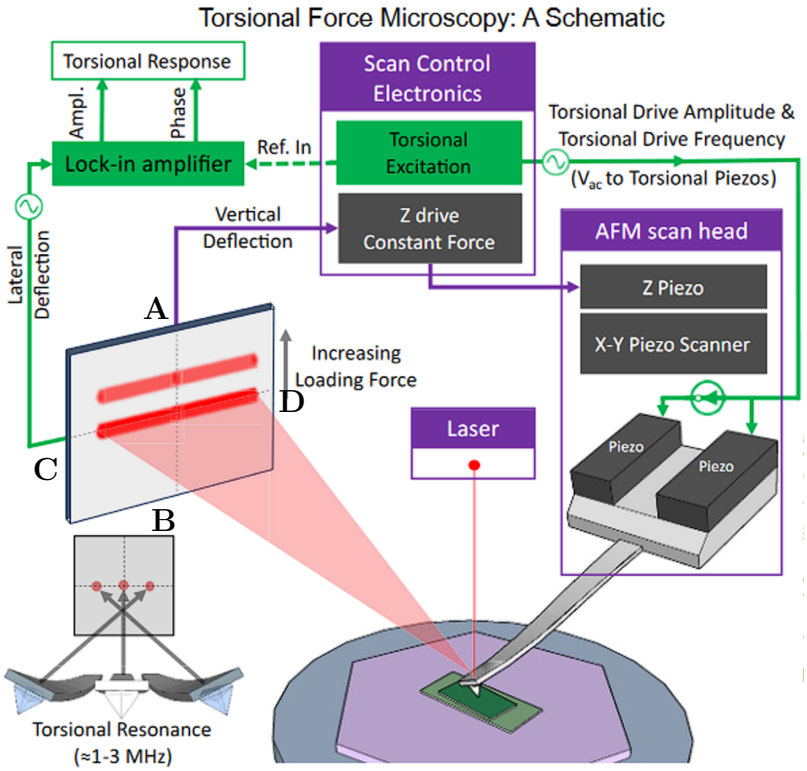

Figure 3.3: *Schematic of TR friction imaging where the two parallel loops are indicated: a closed feedback loop (purple) that tracks topography to maintain constant vertical force, and an open loop (green) that excites torsional resonance to map mechanical response. The TR amplitude or phase, sensitive to dynamic friction from tip-sample interaction, induced by the moiré superpotential, is mapped. The vertical and torsional deflection are detected on the photodiode (left). Adapted from Fig. 1 of [15]*

to dynamic friction arising from the tip-sample interaction, induced by the moiré superpotential, is recorded. This loop follows a similar procedure to non-contact or tapping modes. A lock-in amplifier is used to compare the measured torsional response with the torsional excitation, producing images that map the phase and amplitude shift [15].

The photodiode used in AFM is typically a quadrature photodetector. As seen in Chap. 2.2 the torsional and lateral bending modes are generally positioned at higher frequencies than the vertical bending (Z) mode. Vertical bending of the cantilever is detected by the A-B quadrants, while torsion is detected by the C-D quadrants. However, pure in-plane lateral bending (Y) of the beam-shaped cantilever cannot be detected by this setup. Due to the tip projecting downward from the cantilever's end, what is nominally a lateral bending mode often includes a torsional component, however, it is reasonable to treat the obtained resonance modes as fully torsional [35].

The cantilever's torsional and lateral resonant frequencies may overlap due to fabrication tolerances, leading to the unintentional selection of the lateral bending mode, which has a significantly larger Y displacement. This Y displacement can interfere with the Z-drive movement that maintains constant force [33]. To detect and address the coupling of tor-

sional and vertical bending, a "Coupling check" (see Chap. 4.2 and App. A) is performed before measuring, and if necessary, a different torsional mode or cantilever is utilized.

A list of the geometry of the utilized cantilevers is shown in table 3.1. with the uncertainty noted in brackets. As we will discuss in Chap. 4.2 Tap300Al-G, which is a typical tapping mode cantilever, failed to resolve moiré superpotentials. The cantilevers HQ:NSC18Al BS (abbreviated as NSC18) and Asyelec.01-R2 (abbreviated as 01R2), were used in successfully acquired images. Adama AD-2.8-AS is the cantilever that was used in the study of Pendharkar but is also the one selected in the AFM software, since it exhibits similar geometry.

Name	Abbreviation	Force constant k [N/m]	Resonance frequency f [kHz]	Length [µm]	Width [µm]	Thickness [µm]	Height [µm]	Tip radius [nm]	Tip coating
Tap300Al-G									
Tap300Al-G		40 (20 - 75)	300 (200 - 400)	125 (115 - 135)	30 (25 - 35)	4 (3 - 5)	17 (15 - 19)	10	
HQ:NSC18/Al BS									
HQ:NSC18/Al BS	NSC18	2.8 (1.2 - 5.5)	75 (60 - 90)	225 (1-230)	27,5 (24.5 - 30.5)	3 (2.5 - 3.5)	15 (12 - 18)	< 8	
Asyelec.01-R2									
Asyelec.01-R2	01R2	2.8 (1.42 - 5.8)	75 (58 - 97)	240	35	3	12.5 (10 - 15)	25	Ti/Ir
Adama AD-2.8-AS									
Adama AD-2.8-AS		2.8 (1.0 - 6.0)	65 (50 -100)	225 (215 - 235)	35 (30 - 40)	1.5 (1 - 2)	12.5 (10 - 15)	10	

***Table 3.1**: Lists the geometry of different types of cantilevers. Tap300Al-G is the typical tapping mode cantilever, which doesn't resolve the moiré pattern. HQ:NSC18Al BS (abbreviated as NSC18) and Asyelec.01-R2 (abbreviated as 01R2) are the two cantilevers that successfully revealed the moiré superpotential. Adama AD-2.8-AS is the cantilever that was selected in the AFM software with a default deflection sensitivity of 104 nm/N. This cantilever was also utilized in the study by Pendharkar.*

3.2 Sample preparation

For Moiré pattern imaging, most AFM modes require an open surface graphene layer. A dry transfer technique, known as stacking, is employed to place multiple layers of 2D materials on top of each other. The device is created using only a bottom hBN flake as a support for picking up the graphene flake with the dry-transfer technique. Initially, one part of the cut graphene flake is picked up with a soft polymer stamp (see Chap. 3.2.2), the chip is rotated, and then the second part of the graphene flake is picked up. For imaging, the device can remain on the stamp, providing a method for determining the twist angle during the fabrication process[15] (see Chap. 3.1.1). For a visualization of the stacked layers in the device used for imaging, see Fig. 3.4. For later transport experiments the sample has to be fully encapsulated for hBN to ensure a clean tBG, and provided with gates, therefore the full fabrication process extends the process employed in this thesis. A detailed explanation of each step in the fabrication of tBG devices is provided below.

These methods are primarily based on developments by [43], [44] and were further tried to be optimized towards a high yield, similar to [14].

Figure 3.4: *Schematic image of the layers of the device used for moiré imaging. The tBG (indicated as yellow and purple Gr) is picked up with hBN and is left on a stamp made of soft polymers polycarbonate (PC) and Polydimethylsiloxane (PDMS), during the AFM measurements. Adapted from Fig. S6. of [15].*

3.2.1 The exfoliation process

We start by describing the exfoliation process - a method to mechanically extract monolayer graphene flakes and other 2D materials on SiO_2. Since the discovery of exfoliated graphene in 2004 [3], the fabrication method was refined by Hung et al. [45], who developed a protocol. In Ref. [46] the different techniques for extracting graphene were summarized. These extraction approaches can be divided into top-down and bottom-up. The former includes mechanical and chemical exfoliation, while the latter includes chemical vapor deposition (CVD) and epitaxial growth. According to Ref. [45], CVD may lead to the formation of grain boundaries and defects, effects that need optimization. Mechanical exfoliation on the other side can provide a low-cost and high-quality method to extract graphene, but is not suitable for large-scale production. Furthermore, most of the novel quantum effects in graphene were explored on exfoliated graphene underlining its crucial role in extracting 2D materials [45].

Pre exfoliation

Before starting the exfoliation process, it is crucial to thoroughly prepare the substrate, which provides an atomically flat surface to support the graphene and to ensure a high contrast for later graphene flake searches. The preparation involves cutting and cleaning the wafers. Using a Si wafer with a top layer of 285 nm SiO_2 improves the contrast and adhesion between the graphene and substrate [47].

To achieve a small chip size, the edge of the wafer surface is scratched with a diamond scriber, causing enough damage to the crystal structure that it breaks easily along one lattice axis into the desired size of around $1\,cm^2$. The utilized tools are seen in Fig. 3.5. During the cutting-process, the wafers gather dust and small crystal pieces that break apart. Therefore, it is important to clean the cut wafers using pressurized air and plasma cleaning. The latter is particularly effective for removing organic residues and is crucial

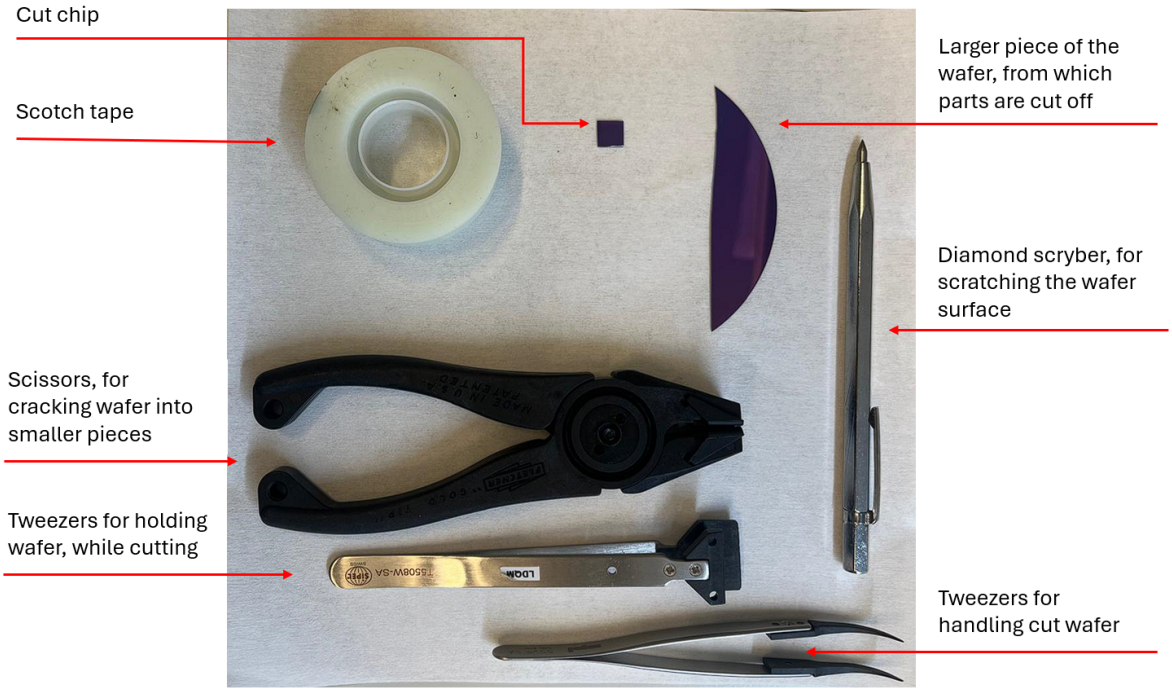

Figure 3.5: *Image of tools utilized for cutting wafers, as well as the Scotch tape employed for exfoliation.*

to exfoliate graphene [45] reliably. If the chips are heavily covered with adsorbates, cleaning in a bath of Acetone and Isopropanol (IPA) helps to provide a clean surface without leaving residues [48].

The plasma cleaning should be performed just before placing the chips on the exfoliation tape. It's important to note that after applying the plasma cleaning process, the silicon tends to attract water molecules, which can lead to poor adhesion and a low yield of graphene flakes [45]. Plasma cleaning is standard practice, and more details about the underlying principles can be found in [49]. To produce O_2 plasma, electrons are accelerated to create ions and radicals in the low-pressure gas. This plasma is then directed onto the surface of the SiO_2/Si wafer and reacts with it, particularly with organic residues on top of the surface (see Fig. 3.6 (b)). We treated the surface with O_2 plasma at 5 Pa for 2-3 minutes.

Furthermore, it was shown that using O_2 plasma for a few minutes is the most suitable plasma form for exfoliating graphene and other 2D materials since it does not negatively affect the adhesion properties of the silicon substrate [45].

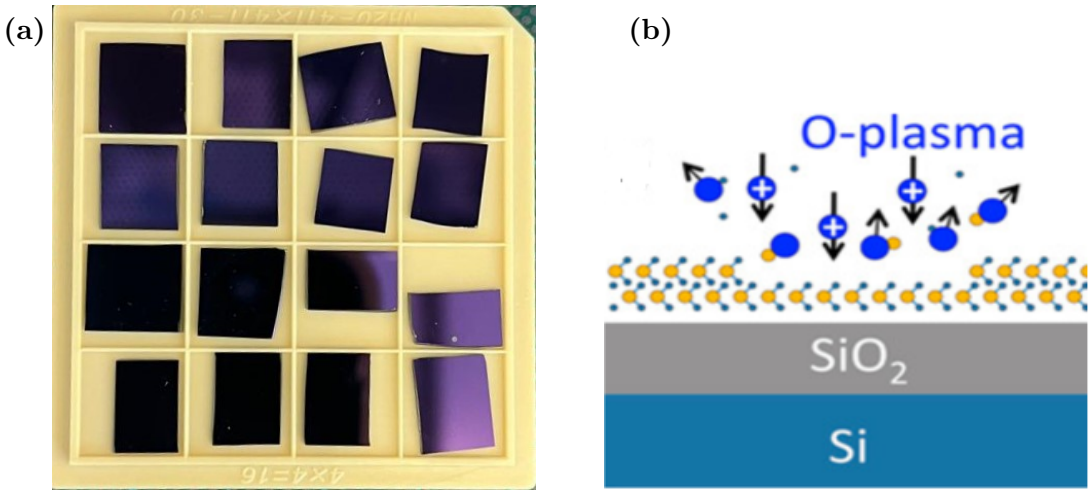

Figure 3.6: *(a) Shwos cut wafers used as exfoliation substrate. Pieces at the top right and bottom right positions demonstrate why cleaning by pressurized air and plasma etching is crucial. Such residuals would lead to issues in the fabrication process. (b) Interaction of O_2 plasma with organic residues on the surface of a SiO_2/Si wafer. Adapted from Fig. 5 of [45].*

Exfoliation - A step by step guide

The following paragraphs will provide step-by-step instructions on the exfoliation of graphene, based on [45]. The exfoliation procedure begins with placing fairly large pieces of bulk material on one end of ordinary adhesive (Scotch) tape. Specifically, when extracting hBN and graphene, we use hBN bulk crystal and graphite, respectively. This step deposits a significant number of graphite layers onto the tape. Folding the tape approximately ten times fully covers it with small pieces of graphite, which break into thinner layers with each fold. It's important to note that excessive folding results in small crystals that can negatively impact the size of the graphene flakes. To further reduce the thickness of the graphite, 2-3 uncovered tapes are placed subsequently and exfoliated on top of the covered tape.

We then continue with the exfoliation process, by placing the etched chips on the desired areas. We apply as much force as possible by hand on the backside of the chips to improve the adhesion between the graphene and the SiO_2/Si chips. The tape with the attached chips is then placed on a hot plate at $\sim$ 100-110°C for 3-5 minutes. Finally, the tape is removed by gently pulling upwards while holding the chips stable with tweezers and then placing them in a container.

It's important to recognize that this process combines both randomness and skill. The randomness is inherent, as exfoliation consistently produces a mix of mono-, bi-, and multilayers. However, experience is crucial, as the outcome is influenced by numerous unquantifiable factors, such as the applied force and the degree and manner of folding.

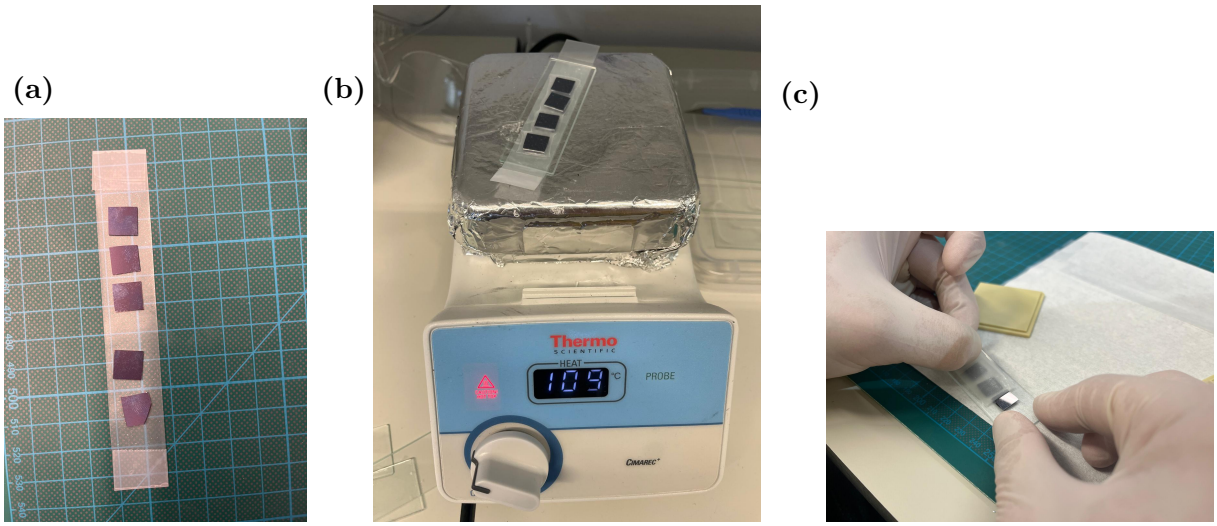

Figure 3.7: *(a) The wafers are placed on a Scotch tape full of the desired crystals, here hBN bulk crystal. (b) After applying pressure by hand, the tape with the wafers is heated at ∼ 100-110°C for 3-5 minutes, accordingly to [45]. (c) Removing the tape by slowly pulling up and holding the chip in place (here hBN exfoliation).*

Flake search

To systematically search for previously exfoliated graphene (see Chap. 3.2.1) on the SiO_2/Si chips, we use an optical microscope with 5-50x magnification. The aim is to create a catalog of promising graphene flakes by saving an image and location on the chip as a simple map. This will help in planning the stacking process, as described in Chap. 3.2.2. Figure 3.8 shows the microscope setup used for flake search and stacking. When light reflects off the flakes, it alters its path, creating a color contrast between the flakes and the substrate and a distinct contour line. To optimize this contrast, the oxide layer on the chip should be ~ 285 nm thick, according to [47] which is based on the Fresnel law. An optical image of the flake is projected onto the camera, allowing the measurement of distances, and intensity profiles, and the drawing of an outline of the flake. The utilized oxide layer thickness imposes a green light source or green filter for high contrast [47]. The intensity profile lowers above a flake compared to the surrounding SiO_2, because of the change in contrast, which is approximately proportional to the number of layers. At this specific thickness not only monolayers can be detected but also most few layers (≤ 10 layers) exhibit high contrast [50]. This enables the distinction between mono- and bilayers and few-layer graphene [47, 50]. The search for potential flakes begins at 5x magnification and systematically covers the entire chip using a grid search method manually. When a potential flake is found, further documentation and confirmation of it being a promising graphene flake are done using 20x and 50x magnification. Figures 3.9 (a) and 3.9 (b) are examples of documentation, done by saving the image and its location on the chip. The importance of the flake search should not be underestimated, since it's the preparation for later stacking.

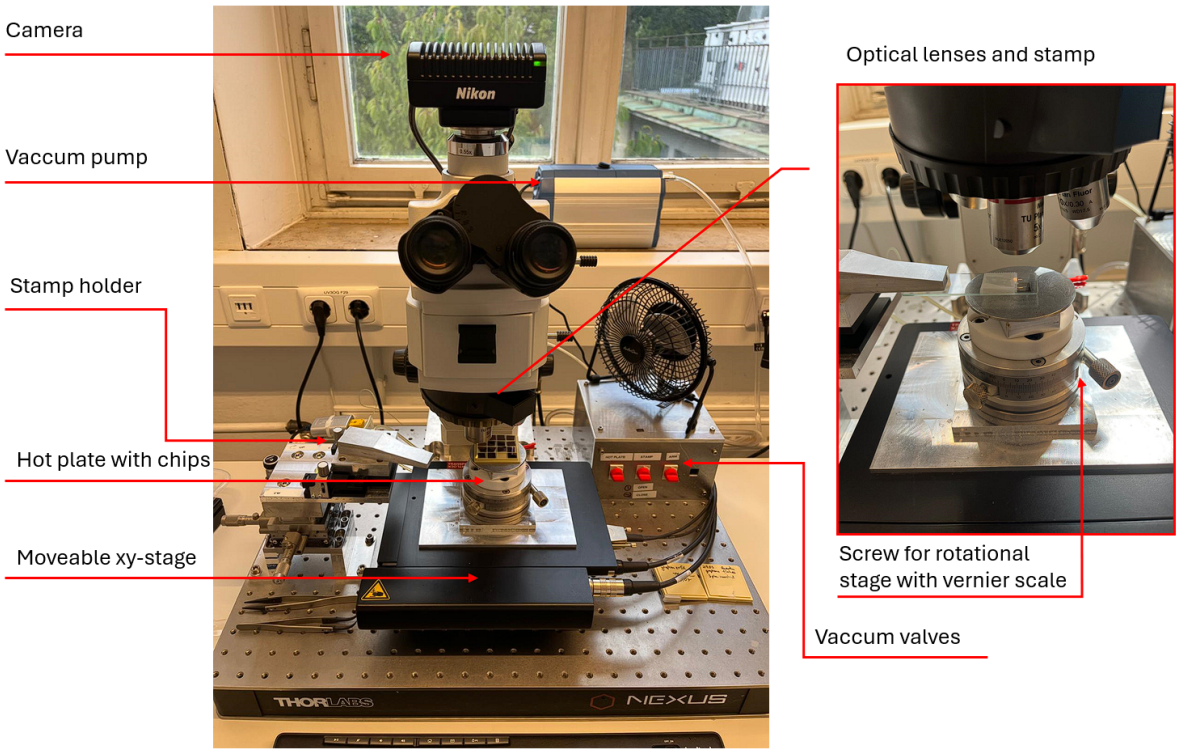

Figure 3.8: *This is the setup of the microscope, used for flake search and stacking with an enlarged view on the hot plate and stamp. The vacuum pump is used to attach the stamp and the chip to the holder and hot plate respectively. The hot plate can be heated and is used to increase adhesion between the stamp and graphene/hBN and reduce the amount of trapped bubbles in between the flakes. The table is moveable and also the height, position, and tilting of the stamp can be adjusted by screws. The enlarged view shows the screw which is used for rotating the plate to obtain a twist between two layers of graphene. High precision can be obtained through the vernier scale.*

3.2.2 Stacking

We will now discuss the steps to fabricate a tBG using PC as an adhesive polymer stamp, which is based on work done by Zomer [43].

Planning a stack

The planning starts by selecting a flake from the catalog, described in Chap. 3.2.1. To choose a viable graphene flake, several critical factors must be considered. Firstly, the flake should have sharp edges. This makes the appearance of a homogeneous crystallographic orientation, which is essential for consistent and predictable properties, more likely. Secondly, the flake must be free from step terraces and tape residues, as these imperfections can significantly affect the flake's quality and performance [14]. Lastly, it is important to remove any nearby flakes to prevent complications during the stacking process (see Chap. 3.2.2). These nearby flakes can interfere with the stacking, leading to defects or even losing the final device. We aimed to use sizes of graphene flakes that are

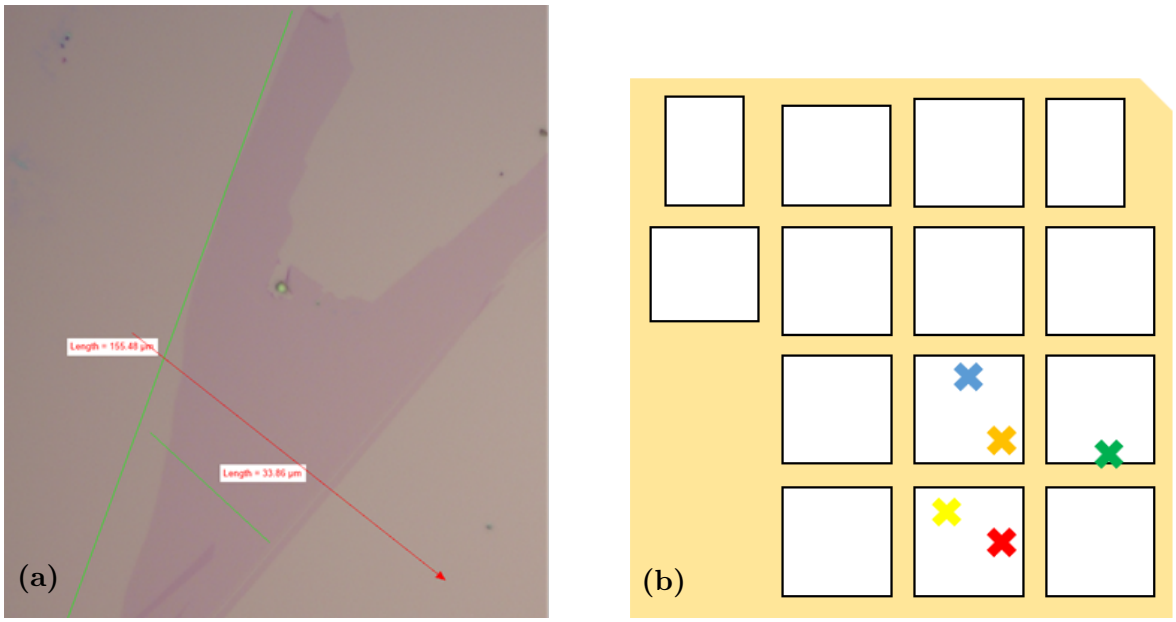

Figure 3.9: *(a) shows a promising graphene flake, top right part later used for device 1. (b) shows a map of the location of the flake search. The yellow background represents the box, in which the chips are stored. The white squares represent the chip and the cross is the approximate position of the graphene flake.*

commonly used in later measurements and Hall bar devices, namely sizes of 10 - 20 µm by 20 - 30 µm, to demonstrate moiré imaging for an applicable use case.

It is important to select the right hBN flake to ensure a high device yield. The flake should have at least one sharp edge that can be aligned with the cut edge of the graphene flake, acting as an "anchor" [14]. As described in [14], achieving a target twist-angle accurately is challenging due to the weak vdW-bonds between the sheets and the tBG being only energetically stable in AB stacking at $\theta = 0°$. In addition, the two flakes move with respect to each other in an uncontrolled manner, influenced by the forces of the stamp during the pickup process. As a result, this creates relative motion, potentially leading to AB stacking configuration that does not display a moiré pattern (see Chap. 3.3.1).

In [51] they utilized the slippery interfaces between two graphene sheets by mechanically twisting them with an AFM cantilever and a built-in gear. This allowed them to adjust the twist angle within a single device between multiple measurements. We aim to set the twist angle to a constant value and achieve an angle close to the Magic Angle with precision. This can be accomplished by aligning the edge of the two graphene flakes with the sharp edge of the hBN flake (see Fig. 3.2.2 (a)). The graphene will then fold over each other, and through the anchoring effect of the aligned edges, the desired twist angle will be locked in place. This clamping method significantly enhances the chance of twisted devices. As described in the Discussion in Chap. 4.3.4, it's still very challenging to achieve a BG with $\theta \neq 0$ and even more challenging to achieve a device at a desired angle.

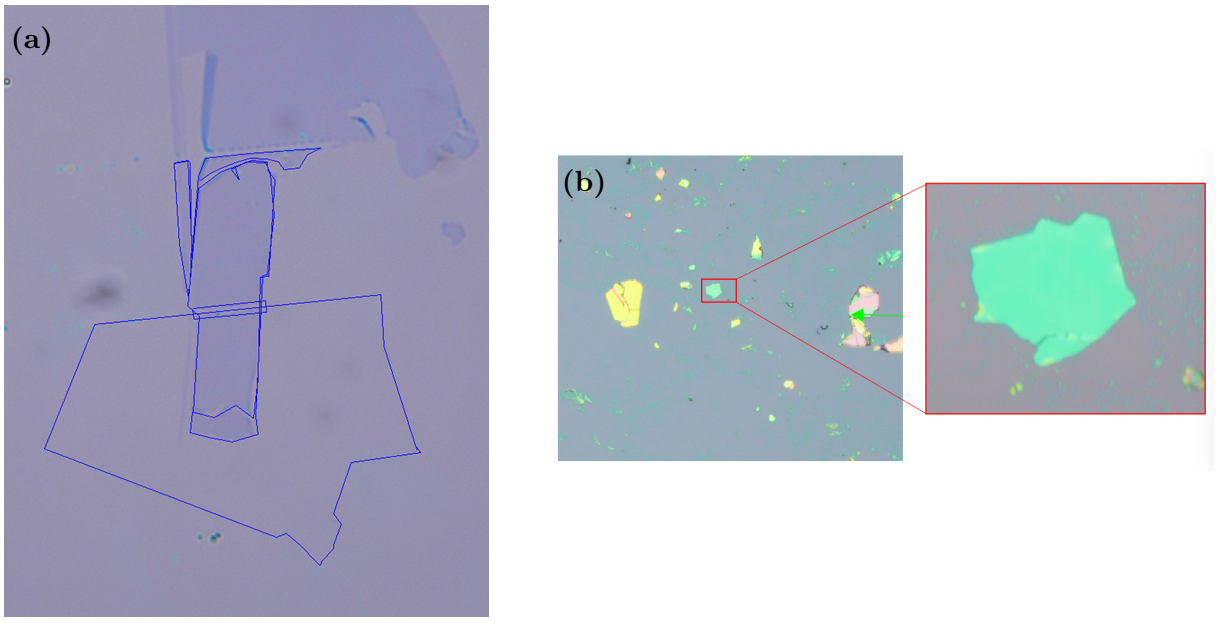

Figure 3.10: *(a) Plan of the stacking process (here device number 1). In the microscope software shapes can be drawn, such that one can see if the flakes, yet on different wafers, fit the geometry. The bottom outline shows the geometry of the hBN flake with a sharp edge used for anchoring. (b) hBN flakes on SiO_2/Si (here used for device number 2). All nearby flakes have to be removed with a cantilever. On the right, the sharp edge without any residues can be seen.*

The hBN flake should generally be larger than the graphene flakes and should be chosen to match the geometry of the two flakes. According to [14] it is recommended to use thin flakes (10-20nm), as thinner flakes are more elastic. This is important for a smoother stacking process and to avoid sudden movements that could lead to angle inhomogeneity and strain, which is introduced through the formation of bubbles. Due to the specific contrast of thin flakes, they show a turquoise color under the microscope (see Fig. 3.2.2 (b)). For further discussion of the actual devices, we have fabricated throughout this study, see the results chapter.

Building the stamps

For the stacking process, a polymer stamp is used. It consists of a layer of polydimethylsiloxane (PDMS) and polycarbonate (PC) placed on a standard laboratory glass slide. The PDMS acts as a viscoelastic substrate, and the PC acts as a highly adhesive layer with high glass transition temperature T_g. This enables stacking at higher temperatures compared to other polymers [14]. To create the stamp, a thin layer of polycarbonate (PC) was first extracted. A few drops of a 6 % PC solution in chloroform were placed on a glass slide and evenly spread with another glass slide to form a uniform thin film. The film was then heated on a plate heater at 150°C for 1 minute. The most effective stamps were achieved when the PC layer exhibited to be wrinkle-free, bubble-free, and completely transparent.

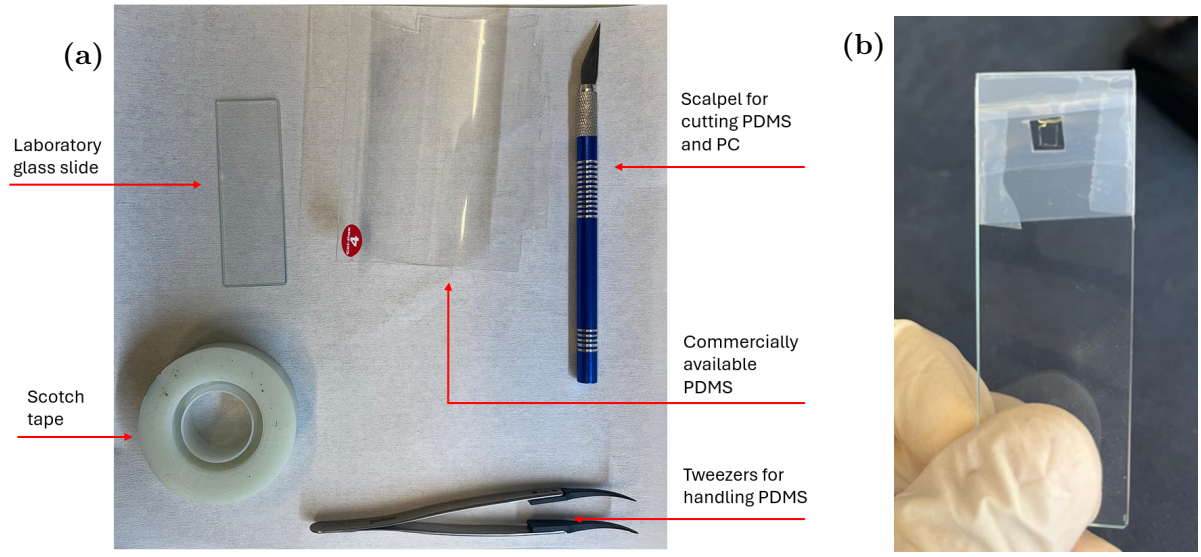

Figure 3.11: *(a) The tools utilized for building the stamps and cutting devices. (b) A stamp with PC, fixed by tape on a PDMS piece on a glass slide.*

We proceed by placing a small ($\sim$ 5 x 5 mm) rectangular piece of PDMS on the glass slide, where it adheres to the surface without assistance. It must be cleaned with ozone plasma for 5 minutes. The PC is cut with a scalpel into pieces that are roughly 2-3x the size of the PDMS. Areas with wrinkles can be spared out. To fixate the PC film, we cut a hole that is 1 mm bigger on each side than the piece of PDMS into a conventional tape. The tape is used to pick up the PC film, place it, and lock it on top of the PDMS piece. For all tools utilized in this process see Fig. 3.11. This process of stacking and building stamps is based on work by Zomer [43].

The final stamp should not have any parts of the tape overlapping the PDMS edge, nor should there be any bubbles or particles between the two polymers, nor should there be any wrinkles. These are the three key factors of the stamp production process that affect the stacking process and, therefore, the final device.

Cutting and removing nearby flakes

After creating stamps, selecting the appropriate hBN and graphene flakes, and planning the stacking process, the graphene needs to be cut into two pieces, with nearby flakes being removed. This cutting process ensures that the two graphene flakes have the same crystallographic orientation. In this study, a mechanical approach is used for cutting, employing a sharp AFM-cantilever that separates the graphene into two pieces with a $\sim$ 1 µm gap. If only a specific part of the flake is of interest, a second cut can be made to separate the desired portion from the remaining graphene. The cantilever is positioned on a PDMS piece on a glass slide and secured with tape to be angled downwards at approximately 10-20° with respect to the glass (horizontal axis). For a full description of the microscope setup see Fig. 3.8.

For a clean and precise cut, the cantilever must be relatively new and should not be used for removing flakes simultaneously. The cantilever is gently lowered onto the silicon substrate at room temperature until it bends, signified by a change in color to shiny gold. Subsequently, it is positioned near the graphene flake according to the stacking plan and swiftly moved over the graphene (see Fig. 3.12 (a)). Applying too much force can cause the cantilever to break, while too little force or using a cantilever previously used for removing flakes can cause the graphene to crumple. For an example of post cut graphene, see Fig. 3.12 (b).

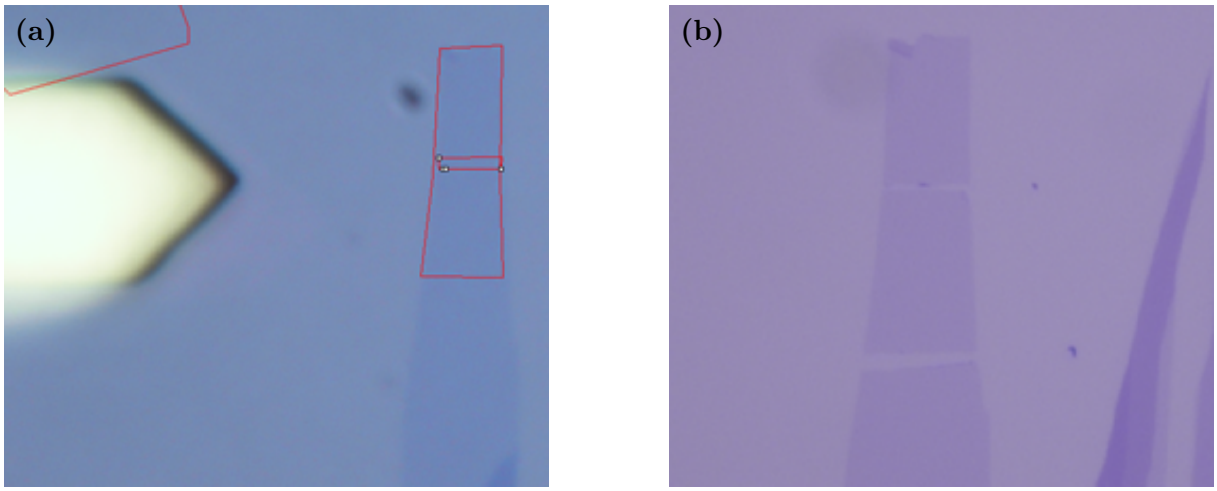

Figure 3.12: *(a) The shiny gold color of the cantilever because of the bending before a cut of a graphene flake. The middle of the cantilever where the tip sits is positioned such that a cut will happen at the planned location. (b) Microscopic image of the two flakes that will be picked up (here used for device number 2). The gap is around 1* µm *and no crumpling happened.*

We used long ($\sim 200\,\mu m$) arrow cantilevers (with an arrow-shaped free end), and because their bending is more controllable than short ones, and the tip is directly positioned below the center, making precise positioning easy. The flakes around the pick-up area can interfere with the stacking process and need to be removed (see Fig. 3.2.2 (b)). We can remove the flakes by either picking them up or pushing them away. We mostly use the pushing method because it utilizes the same kind of cutting device. By applying less force and pushing against thicker flakes, they fold and stick to the cantilever, allowing for complete removal.

Pick up

As described in Chap. 3.2 and seen in Fig. 3.4 we first pick up the hBN that was chosen according to Chap. 3.2.2. The hBN is a support since the graphene adheres more to the SiO_2 than to the PC, so the transfer may be more difficult. Additionally, the hBN provides an atomically flat surface. The cut graphene flakes (see Chap. 3.2.2) are then picked up one by one and slightly twisted with respect to each other.

The chip and stamp are held in place by vacuum, and the hot plate heater maintains a constant temperature of around 110°C. On the left side of the transferstage (see Fig. 3.8),

there are screws that allow the stamp to be manually positioned in the x, y, and z directions, as well as tilted slightly. Tilt control is important for achieving greater precision since the wavefront approaching the flake is more gradual and the wavefront direction is parallel to the cut and sharp edge of hBN. It also allows the contact to be made closer to the edge of the PDMS rather than in the middle.

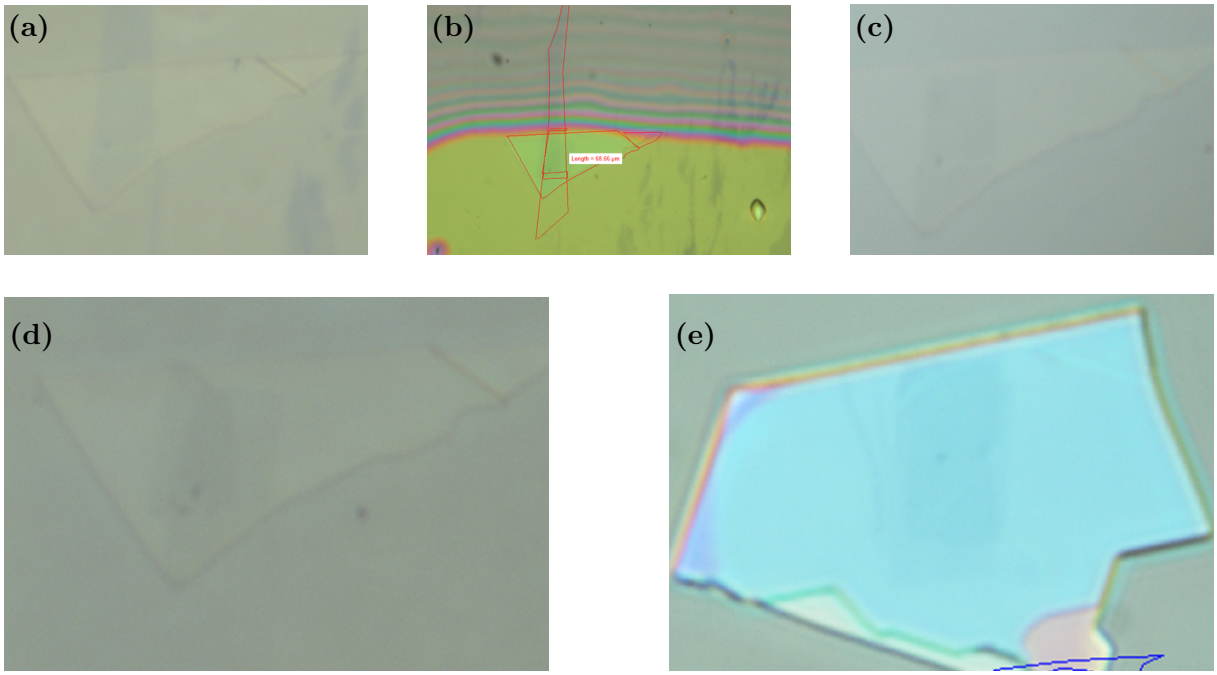

Figure 3.13: *Images showing a stacking process. (a) The already picked-up hBN is lowered with the stamp on the first graphene flake, and the focus of both graphene and hBN shows that the contact is almost made (here device number 3). (b) Wavefront dividing the area with and without contact of the pick-up of the second flake. The alignment of the sharp edge of the hBN with the graphene cut for clamping can be achieved by using outlines. (c) The gray part indicates the first graphene sheet on the hBN after pickup. (d) The dark gray part in the middle shows the overlapping part of the two graphene sheets (tBG), with a gap between graphene and hBN edge. (e)The aligned edges of graphene and hBN of device number 1.*

To properly position the stamp, its x- and y-direction were adjusted so that the lowest corner is near the hBN flake using the tilting screws. Selecting a clean area without any wrinkles and bubbles on the stamp is crucial.
When the stamp is positioned correctly, it is lowered towards the wafer's surface. The focus is kept between the wafer's surface and the stamp to avoid sudden contact. A color change indicates contact and the border between contact and non-contact is called the wavefront as seen in Fig. 3.13 (b). The stamp is lowered to carefully spread the wavefront and extend the contact area. When the desired flake is in the area of contact, the stamp is retracted after about 20-30 seconds. Keeping the focus on the chip's surface immediately shows if the pick-up was successful. If not, the stamp can be lowered again for a longer period, or the temperature can be increased to about 125°C to improve PC adhesion.

After placing the wafer with the graphene below the stamp, the sharp edge of the hBN must be aligned with the cut of the graphene. This alignment can be achieved by carefully lowering the stamp step by step, adjusting the focus between the two surfaces, rotating the plate, and readjusting the position. The outline drawings from the stack planning (see Chap. 3.2.2) can be very helpful. It's recommended to allow the first graphene flake to overlap the edge of the hBN to ensure that it folds over and is clamped on the hBN. When lowering the stamp, it's crucial to be very careful to avoid unintentionally touching the second graphene flake and picking it up next to the stack. Once contact with the first flake is made, the stamp is retracted after a few seconds.

The plate is then rotated by 1.2 - 1.4° since there is a relaxation of around 0.1-0.3° known in the community [14]. For this thesis, demonstrating the capability of AFM moiré imaging on tBG on a polymer stamp, a precise angle, close to the magic angle, is not a deciding factor. It's even easier to resolute a smaller angle since the moiré period diverges towards $\theta = 0°$. For picking up the second graphene flake, the same steps as above are followed and the position of the stamp needs to be readjusted, so the two graphene sheets overlap. The alignment of the second flake with the edge of hBN flake and with that the clamping effect helps to ensure a high precision of the target angle, as described in Chap. 3.2.2. Figures 3.13 (c) and (d) show a gap between the hBN edge and graphene edge, which may lead to an angle relaxation into AB stacking. As already assumed because of the gap we could verify that this device only shows AB stacking (see 4.3.4.

In the whole process, clear documentation is crucial to be able to easily navigate the later AFM measurements toward a promising area on the final device. The clamping process is still very difficult because the graphene flakes tend to move and relax into AB stacking. This issue was faced in devices number one and two, as further described in Chap 4.3.4.

3.3 Post processing of AFM image

In this section, we provide a formula, connecting the twist angle and the moiré periodicity, and briefly discuss the employed algorithms for filtering and Fourier transform. The procedure for obtaining θ is described in Appendix B.

3.3.1 Determining the twist angle

The Introduction, discusses the main goal of moiré imaging, which is to determine the twist angle through observation of the moiré periodicity. It is important to note that there are multiple equivalent formulas available for this purpose. The moiré periodicity is [19], [16], and [52]:

$$d = \frac{a}{2\sin(\theta/2)} = \frac{a}{\sqrt{2-2\cos(\theta)}} \tag{3.1}$$

Here the moiré periodicity is denoted as d and the twist angle between two sheets of graphene as θ. The last equality arises from trigonometric properties [53]. The graphene

lattice constant is denoted as a having a value of 2.46 Å [16]. Rearranging Eq. 3.1, leads to the form which is used in the post processing:

$$\theta = 2 \arcsin\left(\frac{a}{2d}\right) = 2 \arcsin\left(\frac{ax}{4}\right) \tag{3.2}$$

Here we introduced $x \propto \frac{1}{d}$ as the distance between two main Fourierpeaks. The moiré pattern in real space is visualized below in Fig. 3.14 (a) and the divergent behavior of d for $\theta \to 0°$ is plotted in Fig. 3.14 (b).

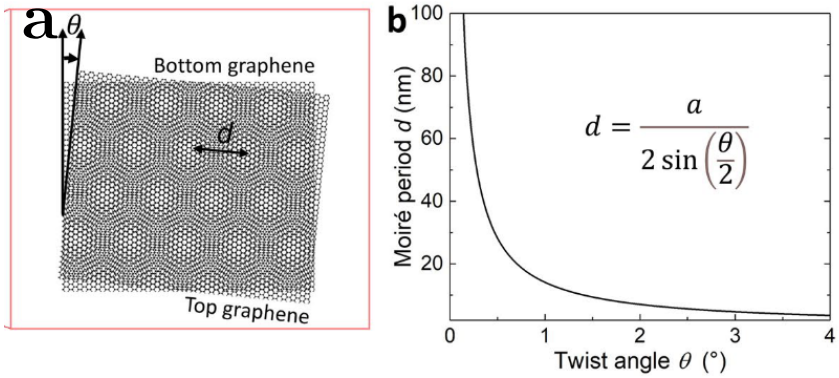

Figure 3.14: *(a): Schematic image of the moiré superlattice exhibited by tBG. (b): The divergent relation between the moiré period d and twist angle θ. Adapted from Fig. 1 of [16].*

3.3.2 2D fast Fourier transform

Post processing moiré images using the software Gwyddion involves several steps to analyze the periodicity of the moiré superlattice. Here, we give a short review of the employed algorithms. The concrete steps, towards the determination of the twist angle, as well as the applied filters, are described in Appendix B. A key part of post processing is applying a two-dimensional fast Fourier transform (2D FFT) to the AFM data. Using 2D FFT is a common way to determine the average periodicity of the moiré pattern [15, 54]. It has the advantage that it allows for the decomposition of complex spatial data into frequency components, thereby providing precise measurements of repeating structures in the image. In the context of crystallographic, the output is an image of the reciprocal space of the moiré pattern.

The FFTW library provided by Gwyddion is employed to perform this transformation efficiently. FFTW is a versatile and widely used algorithm that can handle images of arbitrary sizes. The transformation involves computing the modulus, which is the absolute value of the complex Fourier coefficients. Since a normal discrete Fourier transform (DFT) can be computationally slow, the FFT algorithm provides significant speed improvements, which is crucial for handling large datasets [55]. However, because the Fourier transform assumes the data is infinite and periodic, special "window functions" are applied to prevent spectral leakage caused by sharp discontinuities at the data boundaries. By applying a suitable window function, these edge effects are suppressed, resulting in a more accurate and cleaner Fourier spectrum [56].

Chapter 4

Results

The reader was equipped with the theoretical background on graphene, with emphasis on MATBG and the operation of an AFM, especially the TFM mode. The fabrication process for tBG was described and a detailed SOP for the AFM and postprocessing steps are provided in the Appendix A and B. In the following chapter, the obtained results are presented. Starting with a discussion of issues observed in the calibration of deflection sensitivity and spring constant, we compare torsional resonance curves of different cantilevers and analyze the effects of certain parameters on the image quality.

4.1 Deflection sensitivity calibration

Calibrating the spring constant and deflection sensitivity is crucial to ensure a precise measurement of the applied loading force. This calibration, typically performed in force modes, was used by Pendharkar to accurately convert the deflection signal from millivolts (mV) to force in nanonewtons (nN) [15]. Without proper calibration, there is a risk of applying excessive force, potentially damaging both the sample and the tip. Since these constants can vary slightly between different cantilevers, accurate calibration is essential.

The most common method for determining these constants is thermal tuning, which involves measuring the resonance of thermal noise to calculate the spring constant and is based on [57]. This method can be implemented in various ways, but it fundamentally relies on the precise geometry of the cantilever beam. Thermal tuning is highly sensitive to errors in tip height; a 20% error in tip height, which is common due to fabrication variations, could result in a 20% error in the deflection setpoint and, consequently, the applied force [15]. Pendharkar utilized this method through a custom Python code, which they also provided. However, the code was too complex to implement within the scope of this thesis. In their approach, they acquired the noise data in any AFM mode with all amplifiers turned off, allowing for accurate calibration of the cantilever's properties [35].

We attempted to use the thermal tuning method directly in the AFM software [58], but found it to be highly inaccurate in the utilized way. Despite this, we were still able to effectively image the moiré pattern. With inaccurate deflection sensitivity and spring

constant, the apparent success in obtaining high quality in most images was misleading. Two main issues contributed to this:

- The software allows only for selecting a similar (Adama AD 2.8 AS), but not identical, cantilever model, resulting in significant errors in geometry.
- Accurate calibration of the spring constant requires calculating the correct deflection sensitivity using a stiff sample, such as glass. We did not perform this step, so the software used the default value of 104 nm/N for the selected cantilever.

We identified the erroneous values due to their large variation (100-300%) compared to the spring constant specified in the datasheet. Finally, skipping the thermal tuning calibration step did not affect the quality of the measurements, in fact, the contrast improved and is therefore not included in the instructions of the App. A. As we will see in Chap. 4.3.2 a very high deflection setpoint broadens the domain walls and reduces contrast.

In the following, we report the deflection setpoint in volts (V) instead of force. This value can vary slightly between cantilevers and significantly across different types. It also depends on the alignment of the laser beam on the cantilever. However, since we approximately used the same spot on every cantilever, it can be used as an indication of the applied force. Furthermore, an accurate determination would still have a 30% uncertainty because of the fabrication variation in tip height. We were able to show that this level of precision is not needed for visualizing tBG moiré superpotentials and that this time-consuming calibration step is not essential for effective imaging.

4.2 Discussion of resonance behavior of cantilevers

We used three types of cantilevers, two of which — 01R2 and NSC18 — successfully revealed a moiré superpotential. Beginning with some observations on the setup, we'll explore the different behaviors of these cantilevers, emphasizing the coupling between vertical and torsional modes, as well as the shift in resonance between acquisition in air and during sample interaction. Additionally, we'll compare the experimental findings with the analytical solutions discussed in Chapters 2.2 and 3.1.4.

For measuring the torsional resonance curve, we used the following settings: a lock-in bandwidth at 0.2 kHz to reduce noise, and a drive amplitude of 20 mV to increase the peak amplitude. Occasionally, we performed the acquisition during measurements, while a 16x gain was on, in which case the data needs to be divided by 16 for accurate comparison. In Chap. 3.1.4 the geometry of the used cantilevers is summarized in table 3.1.4. The incompatible cantilever Tap300AL-G, which is usually used in tapping mode ($k \approx 40\,\mathrm{N\,m^{-1}}$, $l \approx 125\,\mu\mathrm{m}$, $f_0 \approx 300\,\mathrm{kHz}$, $r \approx 10\,\mathrm{nm}$) significantly differs from those used in Pendharkar's study [15], which had $k \approx 2.8\,\mathrm{N\,m^{-1}}$ and $l \approx 225\,\mu\mathrm{m}$ and $f_0 \approx 75\,\mathrm{kHz}$. As shown in Figs. 4.1 (a) and (b), the Tap300Al-G exhibited coupling between vertical bending and torsional resonant modes, indicating that a higher-order mode or a different cantilever should be used, as described in Chap. 3.1.4. Figure (a) shows the C-D photodetector output (torsion) and Fig. (b) illustrates the A-B output (bending). The

resonance curves in both plots are positioned closely and are larger in (b) than in (a), indicating a coupling between the two oscillation modes.

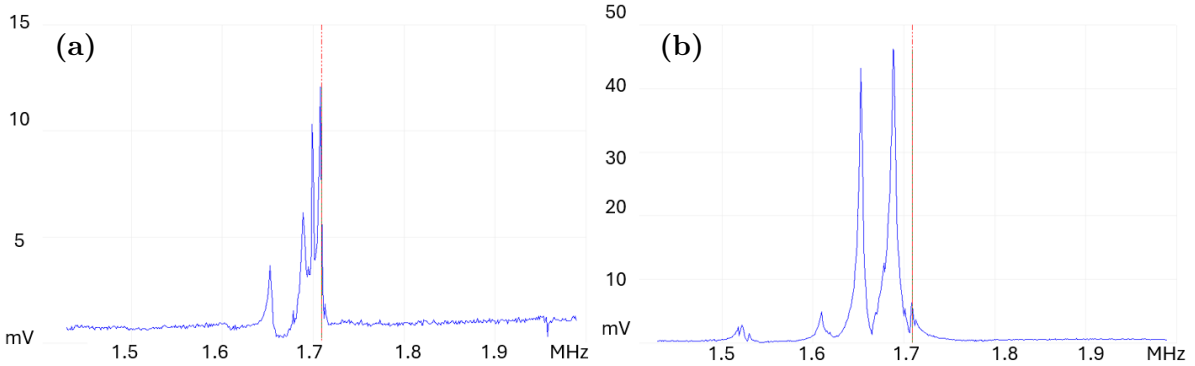

Figure 4.1: *(a) Mechanical response of a typical tapping mode cantilever Tap300Al-G ($k \approx 40\,\mathrm{N\,m^{-1}}$, $l \approx 125\,\mu\mathrm{m}$, $f_0 \approx 300\,\mathrm{kHz}$, $r \approx 10\,\mathrm{nm}$). The red dashed line is positioned at the same frequency of $\sim 1.72\,\mathrm{MHz}$ in both figures but is at the center of the main peak in (a). The comparison of C-D photodetector output in (a) and A-B output in (b) reveals the coupling between vertical bending (b) and torsional modes (a).*

The resonance curves of two different cantilevers of type 01R2 are compared in Fig. 4.2 (a) and (b). The first cantilever (used on Device 1) shows no coupling (see Fig. 4.2 (a)). It exhibits three closely spaced peaks corresponding to different modes, the first of which is selected for measurements. Some of these peaks may represent lateral bending modes, which cannot be distinguished with a quadrature detector as discussed in Chap. 3.1.4. As seen in Fig. 4.2 (b), the second cantilever (used on device 2) also shows no coupling, but the torsional resonances shift slightly, with variations in the relative peak heights. Here the second peak is the most prominent.

In Fig. 4.2 (c) the resonances during measurement are compared to the torsional resonance from (b) (with the y-axis in log scale) revealing that sample interaction broadens and lowers the peak. This makes it difficult to optimize the drive frequency effectively. Furthermore, the consistency of the torsional resonance before and after measurement, indicates that the tip-sample interaction is not permanent, with no evidence of mass exchange or similar effects.

Fig. 4.3 (a) shows that the NSC18 cantilever, compared to the 01R2 in Fig. 4.2, exhibits slightly different torsional resonances. They shift away from 800 kHz and lack additional peaks near the selected resonance. Most cantilevers show a shift to lower frequencies, except for cantilever 3 (green curve), which shows a relatively large amplitude and is therefore scaled by 1/10. Cantilever 1 (red curve) shows the typically selected resonance peak, with no higher-order modes observed. Notably, cantilever 5 was used twice, once with a low resonance at $\sim 620\,\mathrm{kHz}$ and once with a well-defined resonance at $\sim 1080\,\mathrm{kHz}$ (orange curve), both showing no coupling when compared to the vertical bending mode (blue curve).

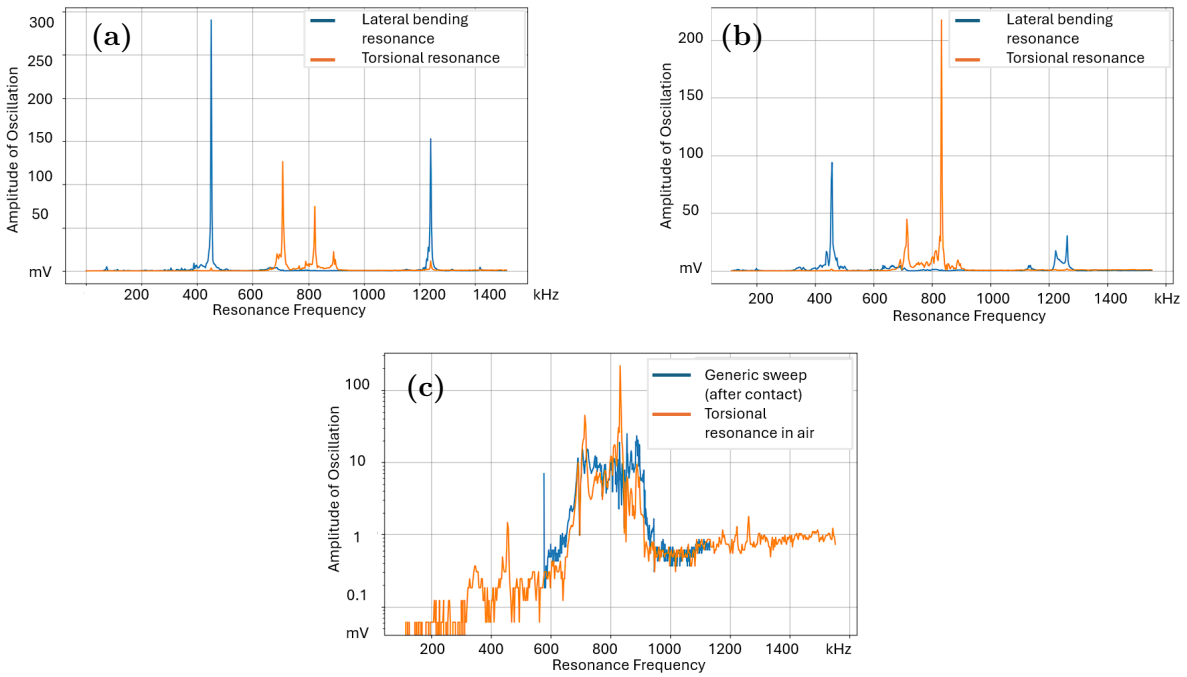

Figure 4.2: *Displays the comparison of resonance curves of two 01R2 cantilevers. (a) shows the first cantilever (on device 1) with no coupling and three closely spaced peaks, the first being selected for measurements. (b) shows the second cantilever (on device 2), also with no coupling, but with shifted torsional resonances and a more prominent second peak. (c) compares the generic sweep to the torsional resonance from (b), revealing peak broadening and lowering due to sample interaction.*

The second resonance mode of this curve (cantilever 5) is detailed Fig. 4.3 (b) details the second torsional mode (blue), compared with the damped resonance curves (green, orange)affected by tip-sample interaction. As anticipated, the resonance shifts to higher frequencies with reduced amplitude, consistent with Pendharkar's findings [15]. However, contrary to expectations, increasing the loading force did not further decrease the peak amplitude. This discrepancy may be attributed to a change in drive amplitude, possibly 24 mV instead of 20 mV. Fig. 4.3 (c) illustrates a similar shift, but smaller, due to tip-sample interaction.

While an analytical approach for calculating resonant frequencies was presented in Chap. 2.2, its accuracy is limited by choosing the right boundary conditions and including the tip. FEM simulations could potentially yield more precise resonant frequencies for an ideal cantilever. However, the inherent variability of each cantilever (as indicated by the large uncertainties from the manufacturer) results in FEM simulations still being approximate. Ultimately, the critical question is whether knowing the exact theoretical torsional resonance would significantly improve the measurement process or moiré contrast. Our findings suggest that moiré contrast remains consistent regardless of whether different resonant peaks are selected on the same cantilever or across different cantilevers and models. The key is to select the highest resonant peak free of coupling. Coupling was only an

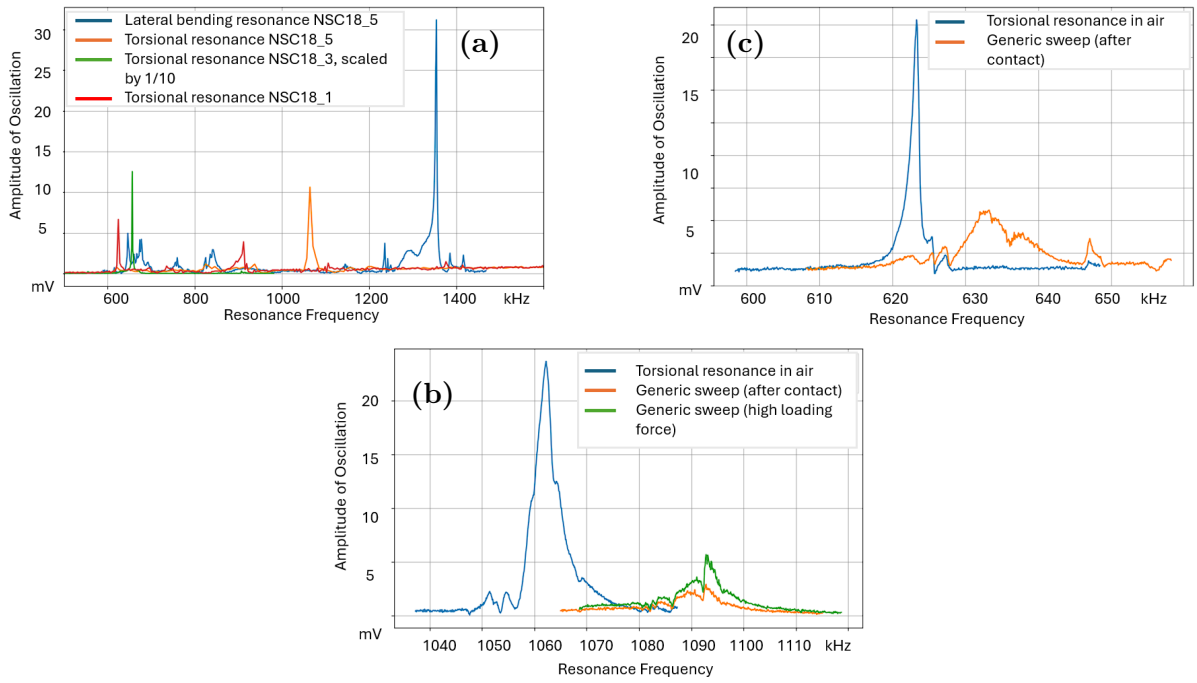

Figure 4.3: *(a) Torsional resonances of the NSC18 cantilever, compared to 01R2, show shifts from* $\sim 800\,\mathrm{kHz}$ *with no additional peaks near the resonance. Cantilever 1 (red curve) displays the typically selected peak, while Cantilever 5 shows varied resonances at* $\sim 620\,\mathrm{kHz}$ *and* $\sim 1080\,\mathrm{kHz}$ *(orange curve), both without coupling (blue curve) and Cantilever 3 (green curve) show a large torsional amplitude, which is scaled by 1/10 for clarity. (b) The second torsional mode (blue) shifts to higher frequencies with lower amplitude due to tip-sample interaction, with amplitude changes between different acquisitions of the current resonance behaviors possibly influenced by varying drive amplitudes and loading force. (c) Displays a similar frequency shift, closer to that of a free cantilever.*

issue with the standard tapping mode cantilever. The observed shift between resonance curves in air and during interaction underscores the importance of the acquisition of the resonance behavior during measurements. Furthermore, because of the use of conductively coated and non-coated tips, we can verify that even though no bias was applied, both types of cantilever yield similar contrast.

4.3 Parameter changes and acquired images

As discussed in the theoretical framework in Chap. 2.1.3, the AA domains appear as regions with a large accumulation of electron density, resulting in the strongest tip-sample interaction at these points. In contrast, AB or BA stacking, which is the natural configuration of graphite, is energetically stable and visually very homogeneous. Here, the electron density is significantly depleted, leading to a minimum in interaction strength. The domain walls between AB and BA stacking, known as saddle points, show higher electron density than AB but lower than the AA configuration. The interaction strength of different regions affects the amplitude and phase of the torsional (see Chap. 3.1.4) oscillation. The amplitude recorded by a voltage on the photodetector is captured at each

pixel and indicated in the color bar. The moiré unit cell is indicated in Fig. 4.4 (a) with AB/BA regions denoted as blue and green triangles, AA configuration as orange dots, and the domain walls (SP) as grey. The reciprocal space (Fig. 4.4 (a),(d)) in the top left corner reveals peaks aligned along three lines, reflecting the periodicity of the moiré pattern and will be explicitly described in part 4.5 of the discussion. Figures 4.4 (b) and (c) show a contrast similar to (a) but with strain and different scan sizes. As illustrated in Fig. 4.4 (e) and (f), the domain walls are less homogeneous compared to the AB/BA configuration.

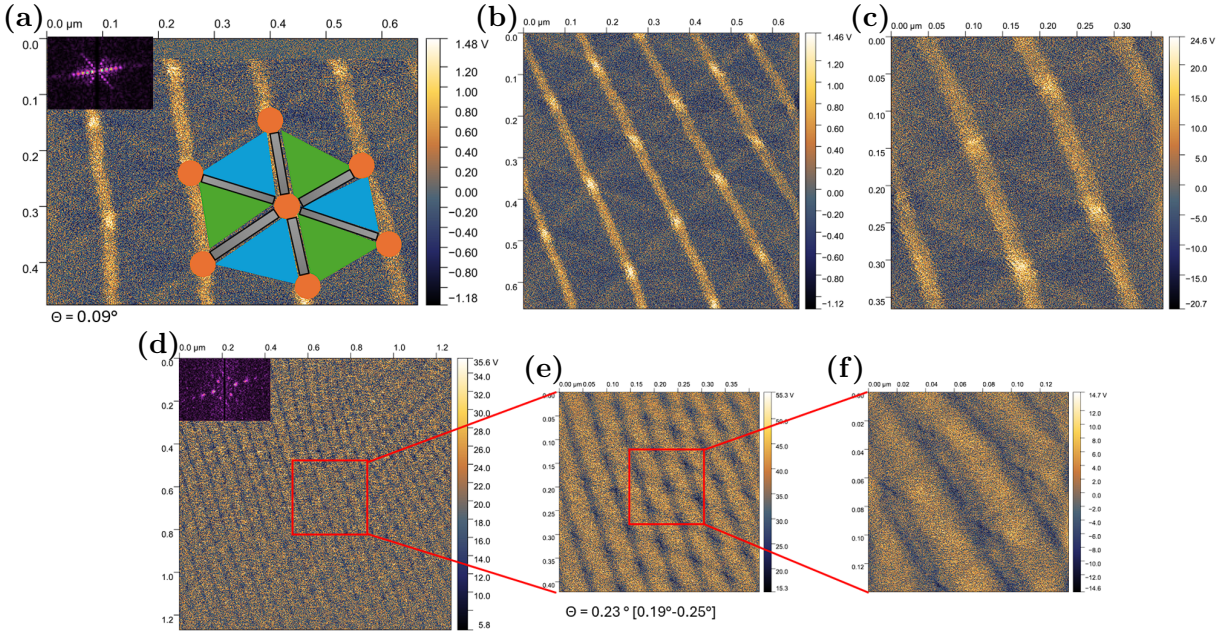

Figure 4.4: *(a) The moiré unit cell with minimal strain highlights AB/BA regions as blue and green triangles, AA configuration as orange dots, and domain walls (SP) in grey. (b)-(c) Contrast similar to a but with strain. 2D FFT of (a), and (d) shows the reciprocal space, positioned at the top left corner respectively, and leads to $\theta = 0.09^\circ$ (a) and $\theta = 0.23^\circ$ (d), thus showing two distinct regions of device 1. The parenthesis indicates the error interval through calculating the angle in all three directions, which may be relatively large due to strain. Images acquired with NSC18, with parameters in (a) [defl.: 0.12 V, scan: 4 Hz, drive: 6 mV, bw: 55 kHz] and (d)-(f) [defl.: 0.09 V, scan: 4 Hz, drive: 12 mV, bw: 10 kHz].*

Although TFM or TR-DFM is generally considered independent of scanning direction [15], [33], domain walls oriented orthogonally to the scanning direction often show higher contrast than others, and in some cases, only these walls are visible. Given that the isotropy of space should hold when TBG experiences zero strain, all lines should appear in the same contrast. This is further supported by multiple images (e.g. Figs. 4.4 (a) and (b)), which typically display all domain walls with nearly uniform contrast. In other AFM techniques, such as PFM [17], samples are manually rotated, and two images are combined to achieve consistent contrast in all directions. However, this approach raises concerns about locating the same spot after rotation, especially without visible markers like bubbles. Additionally, parallel lines alone are usually sufficient for determining the twist angle, and with the mainly used NSC18 cantilevers, all three sets of lines are typically visible.

Device number 1 displays two regions with twist angles of approximately 0.1° and 0.23° (see Figs. 4.4 (a) and (d), both of which are outside the range applicable for MATBG devices but are comparable to the images presented in [17], [18]. Nearly all imaged areas exhibit strain, which influences the calculated twist angle, requiring it to be factored into the uncertainty. In the scope of this thesis, the data were acquired over 15 measuring sessions using two different types of cantilevers (eight cantilevers in total) across four devices, of which only one exhibited a moiré pattern with regions of different amount of strain.

Next, the effects of various parameters and general observations will be discussed, including thermal drift, applied force, scan speed, drive amplitude, and lock-in amplifier bandwidth. As described above the color bar indicates the torsional amplitude as a voltage on the photodetector. We will use the following abbreviations for taking note of the employed parameters for the shown images: deflection setpoint (defl. [V]), scan rate (scan [Hz]), drive amplitude (drive [mV]), lock-in bandwidth (bw [kHz]), e.g. [defl.: 0.09, scan: 4, drive: 12, bw: 10]. The 16x gain was mostly turned on to amplify the signal and improve contrast. Note that the obtained contrast is comparable to the one achieved by McGilly et al. [17]. However, no atomic resolution was obtained, as highlighted in the main source [15], which may be due to the use of softer polymers as substrate.

4.3.1 Determining the twist angle

In this section, we provide images of different regions on device 1. The 2D-FFT and determination of the twist angle is explicitly discussed. Figures 4.5 (a) and (b) display the same area but reveal strain in another direction than for example in Fig. 4.4 (b) and an even smaller twist angle. Comparing these images, which differ in scanning size, confirms that the FFT method accurately determines the angle, as both results in the same value of θ. As outlined in the appendix B, the twist angle is calculated in all three directions and then averaged, with brackets indicating the smallest and largest angles. Averaging only two similar angles or applying a weighting factor can minimize the effect of strain on the calculation, providing an estimate of the angle as it would appear without strain. For minor variations, all three angles can be averaged together. If we had a perfectly triangular lattice over the full image size, we would see six peaks in Fourier space. However, because we have a stretched and nonuniform moiré lattice, we see multiple peaks in the Fourier space, resulting in a reciprocal image that looks more like three intersecting lines (compare Fig. 4.5 (b) and 4.4 (d)).

In the FT image 4.5 (e), three line profiles are placed through the reciprocal space to measure the distance x between two main peaks. One of these line profiles is shown in Fig. 4.5 (f), with x as the distance between the two vertical red lines. This value can then be inserted into Eq. 3.2, which is implemented in a python script. Figure 4.5 (d) presents three lines corresponding to an angle of $\theta = 0.12^{\circ}$ with only minor variations, while Fig. 4.5 (c) displays much thicker lines. These lines still provide a reliable angle determination, as evident when compared to Fig. 4.5 (d).

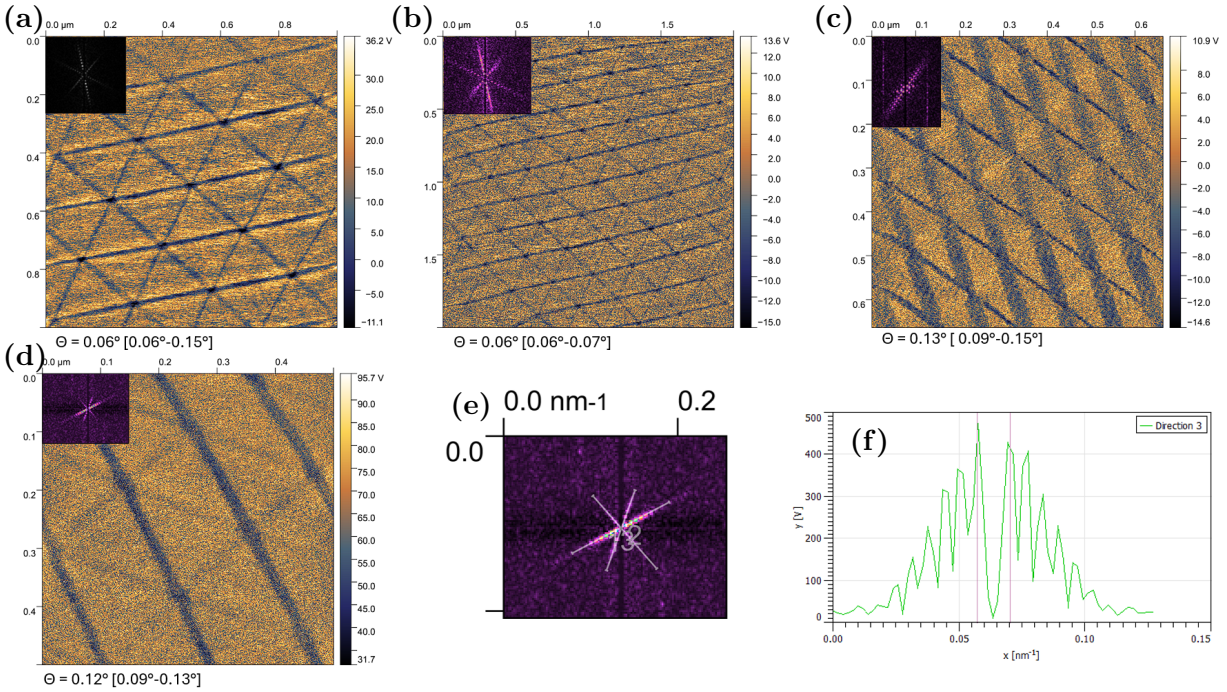

Figure 4.5: *(a) and (b) show strain-induced variations in twist angle at different scan sizes. (c) depicts thicker lines that can still be used for reliable angle determination. (d) shows three domain walls with a twist angle of $\theta = 0.12^{\circ}$. (f) shows a line profile, which is extracted from the reciprocal image (g). Images acquired with NSC18, with parameters in (c) [defl.: 0.8 V, scan: 8 Hz, drive: 22 mV, bw: 67 kHz] and (d) [defl.: 0.09 V, scan: 6 Hz, drive: 12 mV, bw: 55 kHz].*

4.3.2 The effect of deflection setpoint, scan speed, and drive amplitude

According to [15] vertical loading force and drive amplitude (drive) are the most relevant parameters. We will compare different images with relative deflection setpoint (rel. defl.). This is the setpoint subtracted by the setpoint at which the tip loses contact with the surface. Furthermore, we attempt to explain the observed effects, also under consideration of further parameters like scan speed and drive amplitude. However, as described in Chap. 4.1, we are not able to exactly determine the applied force but only the deflection setpoint, which can indicate the magnitude of force. In Fig. 4.6 (b), a higher vertical (rel. defl: 0.25) loading force is used, though still much less than in the case of Fig. 4.7 (b) (rel. defl: 0.75). But compared to an image of the same session, shown in Fig. 4.6 (e) (rel. def: 0.06), which displays more clearly defined domain walls with a force five times weaker, this suggests that the broader lines might result from a combination of higher force but also of increased scan speed.

Figures 4.6 (a) and (d) illustrate two scenarios that can lead to the appearance of a double-lined domain wall, which is not genuine when compared to other images. In (a), the tip may have worn down throughout the measurement due to its silicon composition without coating. This is in contrast to the diamond tips used in Pendharkar's study, where moiré images were still obtained without switching to a fresh tip prior to every measurement

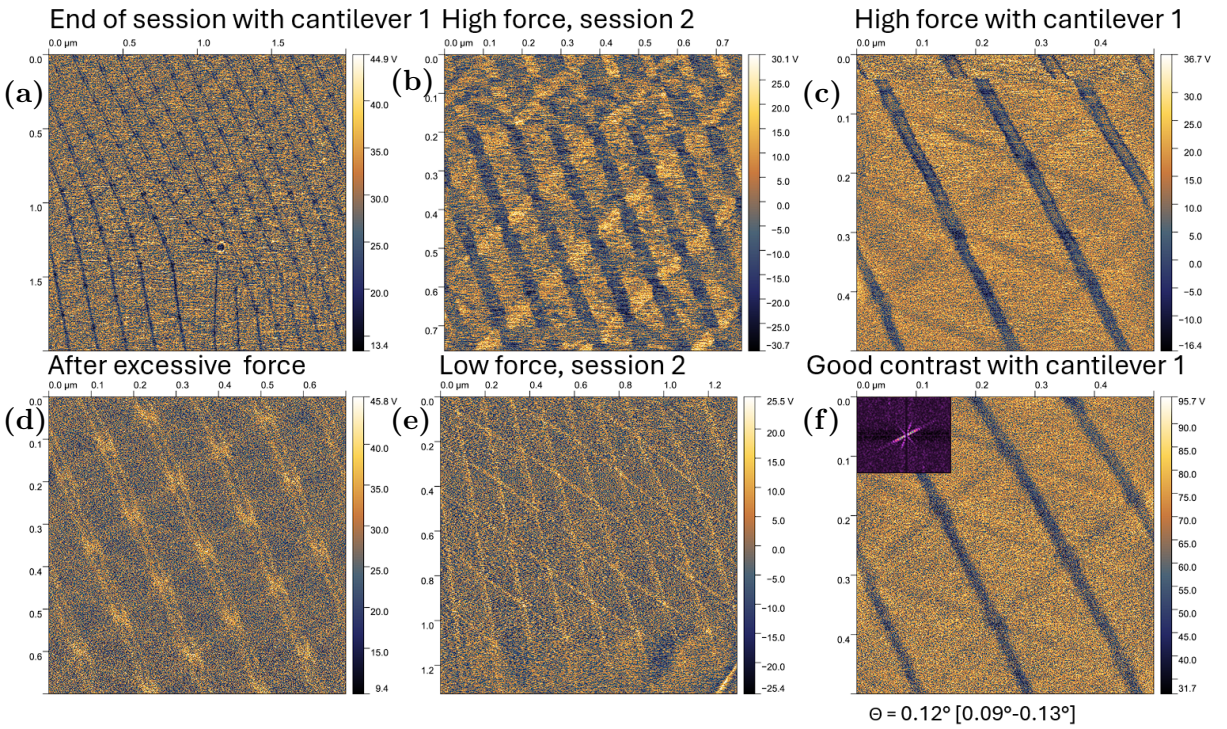

Figure 4.6: *Compares the effects of vertical loading force and drive amplitude on the moiré pattern. (b) and (e) show the impact of different rel. defl. on line thickness and clarity, with (b) using a higher force (0.25) compared to (e) (0.06). The broader lines in (b) may result from a combination of increased force and scan speed. Figures (a) and (d) illustrate scenarios leading to double-lined domain walls, potentially due to tip wear or damage. However, this assumption is contradicted by (c) and (f), where the same tip later produced clearer images. Variations in force rather than tip sharpness are likely responsible for the observed changes, as supported by figures (c), (f), and (e). Note that increasing loading force requires an increase in drive amplitude to maintain contrast. Images acquired with NSC18, with parameters in (b) [rel defl.: 0.25 V, scan: 12 Hz, drive: 25 mV, bw: 90 kHz], (e) [rel. defl.: 0.06 V, scan: 6 Hz, drive: 20 mV, bw: 43 kHz], (c) [rel. defl.: 0.15 V, scan: 6 Hz, drive: 12 mV, bw: 55 kHz].*

[15]. In (d), the tip might be damaged from accidentally applying excessive force. A worn tip may take on a "W" shape instead of a sharp "V", causing the two edges to interact differently and resulting in the appearance of two adjacent domain wall lines, referred to as double lined. However, the assumption that the tip wears down quickly is countered by images 4.6 (c) and (f). After (a) showed double-lined domain walls towards the end of the session, the same tip was used a few days later, yielding the best images obtained (see Fig. 4.4 and 4.5). Increasing the loading force led to the domain walls splitting into two lines (c), but when the force was reduced, the lines merged back into a single domain wall.

If there is a slight vertical drift, potentially resulting in an additional $\sim$ 0.1-0.2V of loading force, the changes observed in session (a) are more likely attributed to variations in force rather than a decrease in tip sharpness. This explanation aligns with observations from Fig. 4.6 (c) and (f), as well as Fig. 4.7 (a) and (b). In the latter, both (a) and (b) employ very high forces (rel. defl: 0.75), probably due to erroneous and thus misleading

determination of deflection sensitivity. Additionally, the scan speed increases from 9.77 Hz in (b) to 16 Hz in (a), which slightly improves the visibility of AA dots but results in even less defined domain walls. However, a vertical drift was usually not observed but may have been overlooked (see Chap. 4.3.3). Furthermore, as the loading force increases, the drive amplitude must also be increased to maintain a similar contrast, as the resonance is dampened by the interaction, which is proved by Fig. 4.7 (a) and (b) compared to (c).

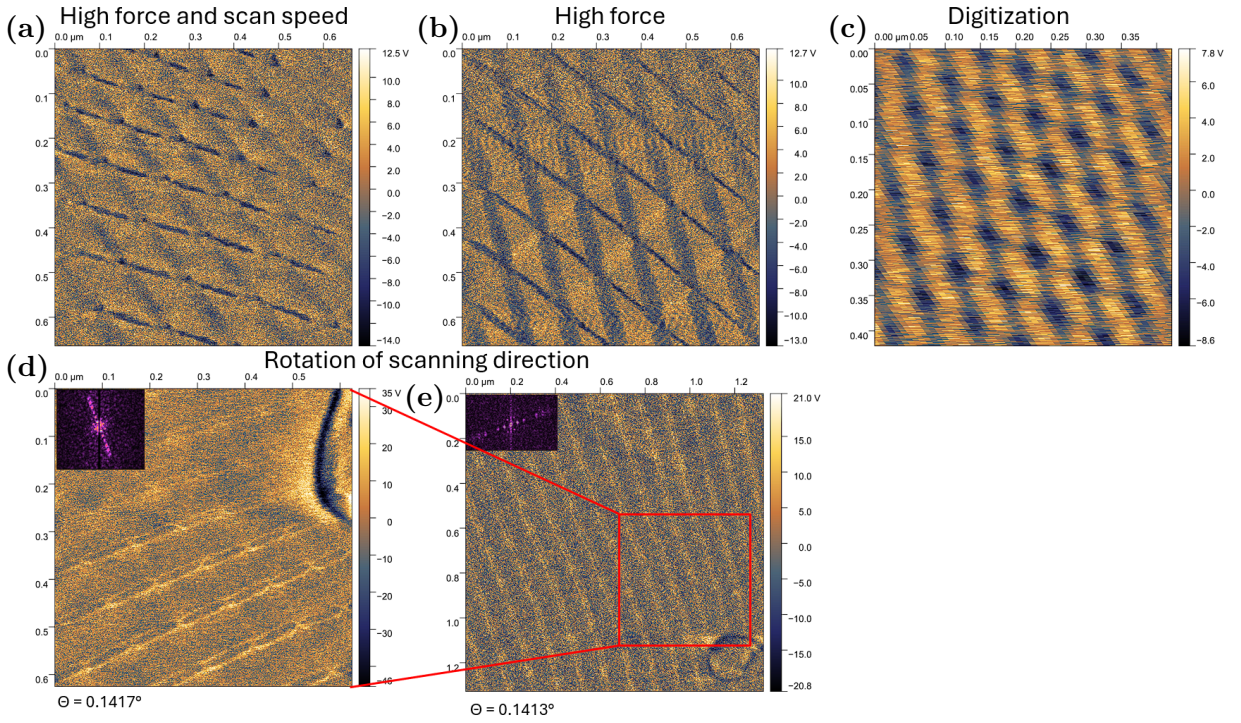

Figure 4.7: *(a) and (b) demonstrate the impact of high forces (rel. defl: 0.75) and increased scan speed (9.77 Hz to 16 Hz). (c) Shows the moiré pattern with a low lock-in bandwidth (0.211 kHz), remaining visible despite digitization effects. (d) and (e) show the effect of rotating the scanning direction by 90°, resulting in rotated and shifted images due to the change in measurement orientation. Nevertheless, only parallel lines can still be used for effectively determining θ. Images acquired with NSC18, with parameters in (a) [rel defl.: 0.75 V, scan: 16 Hz, drive: 30 mV, bw: 67], (b) [rel. defl.: 0.75 V, scan: 9.77 Hz, drive: 30 mV, bw: 67], (c) [rel. defl.: 0.15 V, scan: 6 Hz, drive: 12 mV, bw: 0.211 kHz] and 01R2 (d) [rel. defl.: 0.09 V, scan: 12.2 Hz, drive: 12 mV, bw: 20 kHz], (e) [rel. defl.: 0.06 V, scan: 6 Hz, drive: 6 mV, bw: 40 kHz].*

In fig. 4.7 (d) and (e), the scanning direction is rotated by 90°, which measures perpendicular to the cantilever's long axis rather than parallel, resulting in a 90° rotation of the output image. Consequently, changing this parameter and merging the two images would not capture the entire moiré pattern, as it represents the same signal from the same pronounced domain wall. Additionally, the images are laterally shifted as the mapped position of the bubble is not consistent (and the shape is rotated), leading to a distorted moiré image, which doesn't represent the physical superpotential. However, the angle measurements of $\theta = 0.1417°$ (d) and $\theta = 0.1413°$ (e) are: 1. Reasonable and accurately determined, as compared to Fig. 4.5 (d) and (f), using straight lines, and not the full

pattern; 2. Not affected by the scan size; 3. not influenced by the scan angle, as evidenced by (a) and (b) with scan angles of 20° versus 90°; and 4. not affected by double lined domain walls. Therefore, parallel lines can be used to determine θ, but this method does not visualize strain. Figure 4.7 (c) illustrates the effect of digitization when the lock-in bandwidth is set to a small value (0.211 kHz). Despite this, the underlying moiré pattern remains visible.

In conclusion, regardless of the nature of the changes in mapped domain walls, the images are predominantly sensitive to loading force, scan speed, and drive amplitude, which is in agreement with [15].

4.3.3 Thermal drift of the cantilever

The small bubble, visible in many images, serves as a reference point for orientation. Bubbles influence strain orientation and moiré periodicity, potentially creating areas where the MATBG condition is not met within a 500 nm radius around the bubble [59]. Although this condition is not observed in any region of the device, the presence of disorder around bubbles aligns with literature findings on a similar scale. Additionally, four out of five NSC18 cantilevers exhibit significant horizontal drift, evident from the offset in the photodetector. During 2-3 hours of measurements and calibration, this drift can reach up to 1.5 V. The drift is observable in the varying positions of the bubble across successive images (Fig. 4.8). Each image acquisition takes approximately 90-120 seconds and no manual movement of the tip was employed. The period between the beginning of the first and the end of the third image is approximately 4.5 to 6 minutes, with a 4-minute gap between the first and second image.

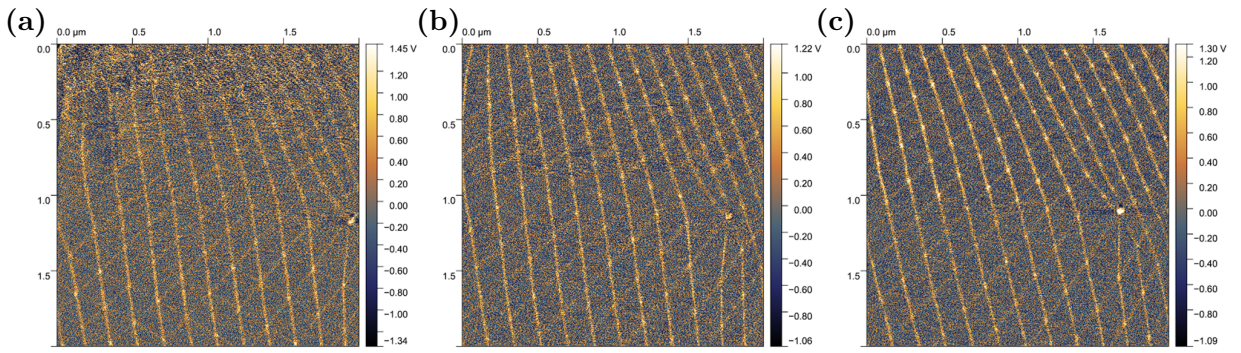

Figure 4.8: *The small bubble, visible across images, serves as an orientation reference and highlights how bubbles can affect strain and moiré periodicity, potentially disrupting the MATBG condition within a 500 nm radius [59]. Four of five NSC18 cantilevers exhibit significant horizontal drift, up to 1.5V over 2-3 hours, affecting bubble positions between images (a)-(c). Minimal drift was noted with the fifth NSC18 and 01R2 cantilever. Vertical drift, impacting loading force, was not observed. Images acquired with NSC18, with parameters in (a), (b) and (c) [rel defl.: 0.12 V, scan: 4 Hz, drive: 6 mV, bw: 55 kHz]*

Drift is a recognized issue in the study of Pendharkar et al. but can be managed by regularly noting horizontal drift [15]. This drift results from the thermal expansion of the

cantilever due to the laser beam used for deflection monitoring and is influenced by the cantilever's material, geometry, coating, and laser alignment. Notably, the fifth NSC18 cantilever showed minimal drift when used for a second measurement a few days later. This discrepancy suggests that the phenomenon requires further investigation. Imaging smaller moiré periodicities, close to the MATBG regime, may be more affected by thermal drift. The 01R2 cantilever exhibited no significant drift, possibly due to its tip and beam coating. Crucially, substantial vertical drift, which directly impacts loading force, was not observed (see the previous discussion of loading force effects, Chap. 4.3.2).

4.3.4 Different domain walls, bubbles and edges

For selecting high-quality regions free of bubbles and wrinkles for subsequent transport measurements, TFM provides a reliable method for mapping these areas (see Chap. 3.1.1 for the underlying motivation). It effectively identifies various features, including multiple bubbles, edges of mono- and bilayer graphene, wrinkles, and domain walls between different regimes of twist angle. Comparing the height (Z-piezo) channel with the amplitude or phase channels helps determine whether visualized features are due to actual height differences or variations between regimes. Typically, changes in height appear as larger changes in amplitude (brighter) and thicker than domain walls observed in the amplitude or phase channels.

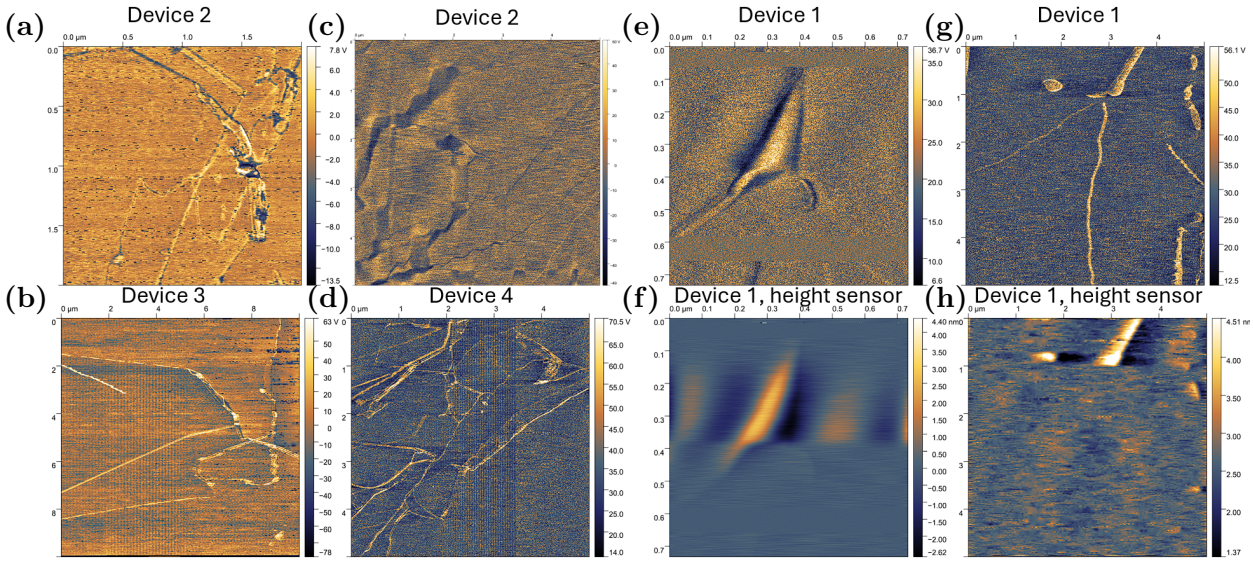

Figure 4.9: *TFM reliably maps high-quality regions free of bubbles and wrinkles for transport measurements. (a) and (c) were obtained on device 2, (b) on device 3 with the 01R2 cantilever, and (d) on device 4. (e) with corresponding height in (f) and (g) with (h) were acquired on device 1 using the NSC18 cantilever. Distinguishing real height variations from domain walls (g) is possible due to the corresponding Z-piezo channel (h).The periodic noise (vertical stripes) in (b) and (d) likely results from fast scan speeds. Devices 2-4 exhibited more domain walls and wrinkles, unlike the homogeneous pattern of device 1, indicating the sample of twisted bilayer graphene might have a cleaner surface.*

We were unable to measure the moiré pattern on devices 2-4, which only displayed domain walls. Despite thorough zooming and using the same cantilever and calibration that successfully measured the first device, no signs of a periodic superpotential were observed on these devices, leading us to conclude that no moiré pattern was present. As noted in [14], the clamping method significantly increases the yield of MATBG devices. We attempted to replicate this process, but the optical image in Fig. 3.13 (d) shows a gap between the edge of the hBN and the graphene layers. This supports our conclusion that devices 2-4 likely relaxed into an AB stacking configuration, which does not exhibit a moiré pattern. Device 1 was aimed to exhibit $\theta = 1.1°$ but only showed regions of $\theta < 0.25°$. As described in Chap. 2.1.2, AB stacking is energetically stable, explaining the shift from small θ towards $\theta = 0°$. From a practical standpoint, the moiré pattern was typically visible at a scan size of 1 µm after adjusting the drive frequency to the shifted resonance peak but without further optimization. This facilitates quick determination if a device lacks a periodic pattern and the decision to discontinue the measurement session. Fig. 4.9 (a) and (c) were obtained on device 2, (b) on device 3 with the 01R2 cantilever, and (d) on device 4 with the NSC18 cantilever. (g) with corresponding height (h) on device 4 and (e), with corresponding height (f) on device 1, both with NSC18 cantilever. The periodic noise (vertical stripes) in Fig. 4.9 (b) and (d) is likely due to fast scan speeds. Typically, changes in height appear as larger changes in amplitude (brighter) and thicker than domain walls observed in the amplitude or phase channels (see Fig. 4.9 (g) and (h)). For device 2, the AFM camera reveals a brighter area and a possible shadow nearby, suggesting the entire stack might be resting on a dust particle, either on the PC or between the PDMS and PC. This uneven surface may have contributed to the lack of an atomically flat interface, promoting the energetic shift towards AB stacking. Interestingly, the devices that did not exhibit a moiré pattern, like devices 2-4, showed more domain walls and wrinkles (see Fig. 4.9 (c) and (d)), whereas device 1 displayed a very homogeneous pattern with minimal domain walls (see Fig. 4.9 (g)). Although we successfully measured the moiré superpotential in only one device, this observation suggests that this sample of twisted bilayer graphene might inherently have a cleaner surface, which is promising for future transport measurements.

The high amplitude feature in Fig. 4.10 (a), barely visible in the height sensor, is thinner and less pronounced than the one in (d), suggesting it is likely a wrinkle, though it could also be a sharp graphene edge. In (b), the enlarged view of (a), a very large moiré period is visible with minimal strain, even adjacent to a wrinkle that is also detected in the Z-sensor. It's noteworthy to observe a large-scale moiré pattern emerging from the edge of the graphene in Fig. 4.10 (c). When examining the corresponding Z-sensor (d), it appears that the bottom part of the image likely represents the transition from bilayer graphene to monolayer and then to just hBN. The wrinkle in the top left corner, visible in the Z-sensor, is more closely examined in (e). This wrinkle separates two regions with different twist angles, with the top region displaying significant strain. In another area of device 1, shown in Fig. 4.10 (f), there is a sudden change in moiré superpotential periodicity and strain direction, occurring without the presence of a wrinkle, graphene edge, or domain wall.

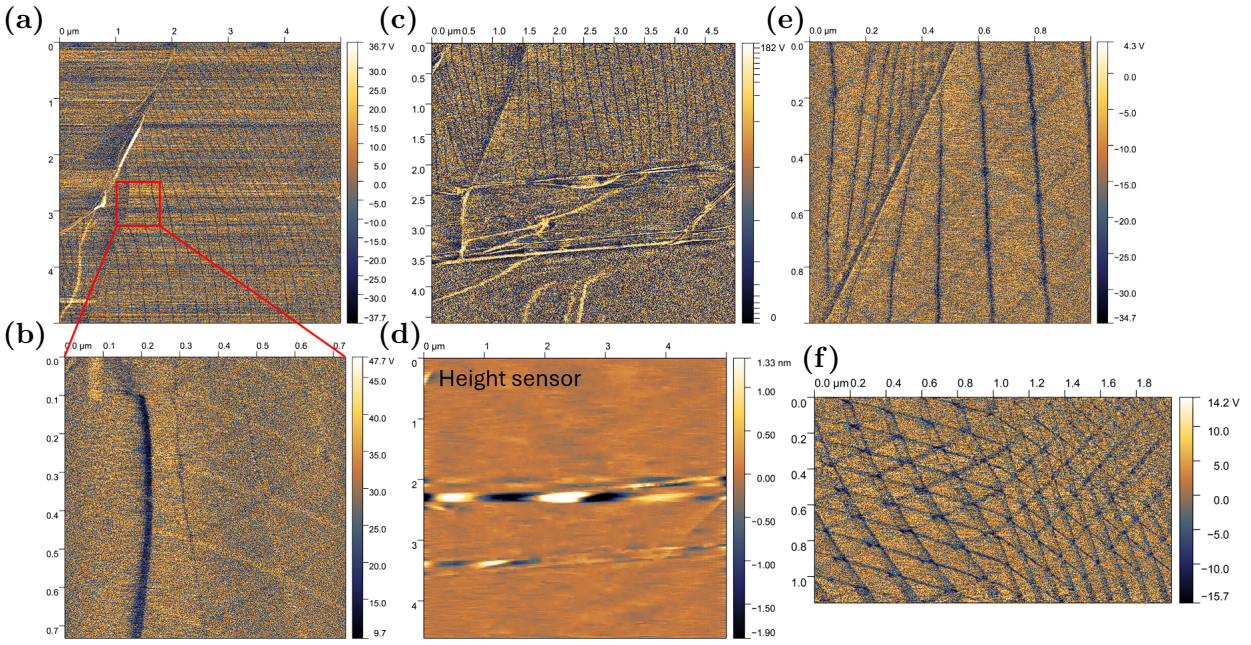

Figure 4.10: *(a) shows a feature of high amplitude, likely a wrinkle, that is less pronounced in the height sensor, with (b) zooming in to reveal a large moiré period with minimal strain. (c) highlights a large-scale moiré pattern emerging from the graphene edge, while (d) indicates a transition from bilayer graphene to monolayer and hBN. The wrinkle in (e) separates regions with different twist angles, and (f) illustrates a sudden change in moiré superpotential periodicity and strain direction without a visible domain wall. Images acquired with NSC18, with parameters in (a),(b) [defl.: 0.05 V, scan: 6 Hz, drive: 12 mV, bw: 67 kHz] and (f) [defl.: 0.6 V, scan: 6 Hz, drive: 30 mV, bw: 67 kHz] and (c)/(d) acquired with 01R2.*

4.3.5 Best parameters

The key parameters influencing image contrast are the deflection setpoint, drive amplitude, and scan speed. After analyzing how variations in these parameters impact image contrast, we recommend the following ranges for achieving high-contrast results:

- Deflection setpoint: 0.05-0.2 V, with ~ 0.1 V providing excellent contrast.
- Drive amplitude: 6-16 mV, where 8-12 mV generally yields good contrast.
- Scan speed: 6-12 Hz, with 6 and 8 Hz being effective for areas of 1-3 µm. For larger areas (> 3 µm), or when measuring the $\theta = 0.23°$ domain of the moiré pattern over areas of 0.5-1.2 µm, reducing the speed to 4 Hz is beneficial.

Additional parameters like lock-in bandwidth showed less impact. For larger areas (1-3µm), a bandwidth of 40-80kHz worked well, with 60kHz being optimal in most cases. For domains with higher twist angles, the bandwidth was reduced to 10kHz, aligning with Pendharkar's findings [15]. "The integral and proportional gain (I and P) is typically set to 1 and 2, respectively.

Chapter 5

General conclusion and outlook

As outlined in the introduction, the motivation for moiré imaging stems from the significance of MATBG devices, which are highly sought after in research but suffer from a lack of reproducibility due to the challenges in precisely controlling the fabrication process—specifically, stacking and twisting two graphene monolayers. This creates an urgent need for a method to accurately characterize the twist angle and assess device quality in terms of bubbles, wrinkles, strain, and homogeneity. Building on the study by Pendharkar, we employed AFM-TFM mode, where the cantilever is driven at its torsional resonance, and the resulting changes in amplitude or phase, caused by dynamic friction, are mapped to visualize the moiré pattern. Unlike PFM and KPFM, this method does not require a conductive substrate, facilitating rapid feedback during fabrication, even when the device remains on a PDMS/PC stamp. The images are then processed with 2D-FFT to determine the average twist angle of the frame.

Compared to previous studies, this thesis explores a broader range of parameters and includes non-optimal images to facilitate discussion and guide replication, making it easier to adapt the method. This approach is further supported by the SOP and a defined range of optimal parameters. Additionally, we offer a comprehensive overview of the AFM setup, the theoretical foundation of moiré superpotentials, and the fabrication process. This thorough approach is designed to assist even those with limited experience in incorporating moiré imaging into their workflow for fabricating MATBG devices.

We successfully identified bubbles, wrinkles, strain, and edges on four different open-surface tBG devices. However, the moiré superpotential was observed on only one of these devices, suggesting that the others likely relaxed to an AB configuration, underscoring the significance of the clamping method during the stacking process. The measured regions exhibited different domains with θ ranging from 0.06° to 0.23°. Given the overall high contrast in small image sizes and the general findings in [17], we substantiate that TFM, using the provided SOP, is effective in imaging moirés near the MATBG condition. The process takes approximately 30 minutes from calibration to obtaining the first moiré image, which is reliable for determining θ, even if the contrast is not yet fully optimized. Mapping the full device across different regions typically requires 1-2 hours.

Logically, the next steps include the demonstration of TFM capabilities for imaging moiré patterns close to the MATBG regime, with periodicities of $\sim 15\,\text{nm}$ instead of $\sim 50 - 100\,\text{nm}$. Given the high resolution, which is comparable to other studies, and the similarity of the utilized cantilevers to the one used by Pendharkar, we are strongly convinced that there are no significant hurdles to image magic angle moiré patterns. However, this capability has to be demonstrated before the process can be easily integrated into the fabrication process. The contrast could be improved by using stiffer polymers or even SiO_2 as substrate. If this is necessary is a question of the use case of the obtained images. As discussed, a lower contrast is already sufficient for just determining the twist angle.

The determination of the deflection sensitivity via thermal tuning should be achieved by employing the method in the code provided by Pendharkar. This gives useful insights into the applied loading force but again is not essential for the successful determination of θ. A direct comparison to other materials, like moiré patterns on graphene-hBN or TMDs would improve the understanding of the differences in frictional properties of these 2D materials. In addition to the deflection sensitivity a translation of the changes in torsional amplitude and phase to the magnitude of friction force would reveal insights into the surface potential of tBG.

An important question that remains is whether θ, strain, and wrinkles change when the second hBN flake is picked up to fully encapsulate the device. This could be confirmed through transport measurements or TEM, which are capable of determining the average twist angle. Moreover, selecting a bubble- and wrinkle-free region necessitates the development of markers that are visible in both optical and atomic force microscopy. Additionally, continuous mapping of moiré lattice inhomogeneities, such as variations in θ and strain, could be achieved by adapting an algorithm previously developed for scanning tunneling microscopy [54]. The TFM mode can also be used to map the moiré superlattices between many other materials, such as TMDs.

We conclude that the SOP will enhance the fabrication process within the community, contributing to advancements in the 2D materials field and future applications in the semiconductor industry.

Appendix A

Standard operating procedure

The standard operating procedure (SOP) closely follows the detailed guidelines provided in the supplementary material of the main paper by Pendharkar et al. [15, 35] and is supported by the manual [58] and TR application note [33] of Bruker. This section will provide a concise step-by-step instruction, summarizing the key steps to achieve a high contrast moiré image. We refer the reader to [35] for more detailed steps that may not be essential.

Setting up the experiment

The basic experimental setup has already been configured and saved as "Torsional Force Microscopy Moire.wks" in a desktop folder, allowing it to be easily reopened whenever TFM for moiré imaging is performed. To begin, launch the Bruker software "Nano Scope V". When the experiment selection window appears, cancel it, then select "Open Experiment" from the "Experiment" menu at the top, and load the saved TFM experiment. The primary adjustments in the experiment compared to the basic TR mode include:

- Setting "Microscope Mode" to "Dynamic Friction" to operate in contact mode-like feedback loops.
- Placing the "Generic Sweep" button in the left column.
- Adjusting the "Engage Setting" for a prolonged approach, that takes approximately 2 minutes to engage.

A logbook template in the form of a spreadsheet for determining the thermal drift of the cantilever and the setpoint of zero loading force has been saved as "Logbook template.xlsx" in the same desktop folder as above. Open the second sheet for a more detailed explanation of the different columns. This template also includes columns for key scan settings, notes, and the saved data file number, recognizing that many settings can be adjusted during measurements. Keeping detailed notes on imaging settings and image quality helps systematically assess the impact of various settings and makes it easier to identify high-quality images during post-processing. An example spreadsheet can be found in Figs. A.2 and A.3.

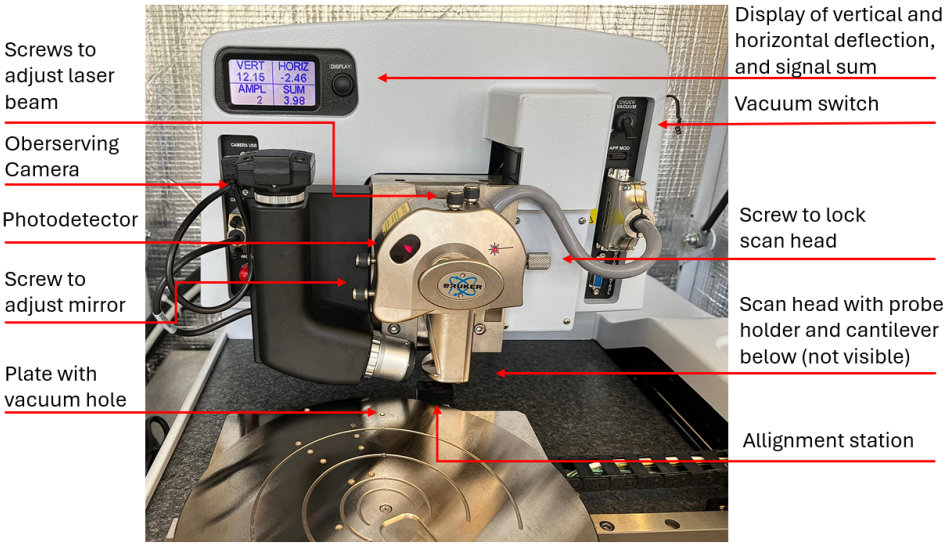

Figure A.1: *Shows the setup of the used AFM, Dimension Icon from Bruker Corp. Throughout the SOP, we will refer frequently to the assigned labels.*

Time	Signal sum	Vertical Deflection	Horizontal Deflection	Flying Condition	Last point of Contact	Snapback	Notes
h	V	V	V	V	V	V	
03:08:00 AM	4,5	0,09	-0,07				a lot of drift
03:22:00 AM	4,5	0,11	-0,2				
				0,1	0,15	0,14	
05:16:00 AM	4,5	0,11	-1,3				

Figure A.2: *Exemplaric logbook for determining the thermal drive of the cantilever and the "Setpoint + 0 nN"*

Image number	Notes	Deflection setpoi	Scan rate	scan angle	samples/line	I and P	16x gain	drive amplitude	TR Lock in BW	
2	NICE	0,21	6	0	512	1 2	Y	20	43	
3		0,45	6	0				22	90	
6		0,55	8							
10		0,5		90						
22				45						
30		0,4	10	0						
31	GREAT		12	0		1 2	Y	25	90	
34										
34	huge	0,4	6	0		2 4	y	24	90	
35	huge, two angles									
36	huge great aa	0,6	6					30	67	
37	smaller nice	0,8	8	0		2 4		22	67	
40	Like 39	0,9	9,77	90		2 4		30	67	
42			16	20						
43	aa dots	0,9	16	20		1 2		30	67	

Figure A.3: *Table with most important parameters to note interesting images with the corresponding settings.*

Prior Scanning

a. Open experiment as described above

b. Attach cantilever to probe holder. For the samples used, neither fresh samples nor fresh tips were necessary to image a moiré pattern or determine the twist angle. However, using a fresh tip improved the contrast.

c. Place the cantilever on the probe holder by first pulling the clamp back. Center the cantilever on the seat, ensuring the beam shows no lateral twist.

d. Attach the probe holder to the scan head by unscrewing the latter and pulling it up. There are four contacts, on which the holder can be stacked. Position the sample on the plate above the vacuum hole so that the glass slide is attracted while ensuring the PDMS is not directly over the hole. Otherwise, achieving proper focus on the sample surface may be difficult. Activate the vacuum pump to secure the sample in place (see Fig. 3.1). The plate can be manually rotated and adjusted in the XY-direction using the software (see step h.)

e. Align the laser on the cantilever

   1. Select "Setup" in the left column, and use "Move to the alignment station" to improve alignment by providing better contrast with a black background.
   2. Focus the observing camera on the cantilever.
   3. Manually align the laser with the screws, seen in Fig. 3.1
      - Adjust the laser spot using the two top screws so that it is positioned directly on the cantilever, aiming to maximize the "sum" (signal sum of all four quadrants of the photodetector). The sensitivity can be tuned by moving the laser incident spot on the cantilever, as the oscillation amplitude is larger at the cantilever free end.
      - Align the mirror, which directs the beam path to the photodetector, using the two screws on the left side. Center the laser beam on the detector to achieve zero horizontal and vertical deflection [(0,0)V]. Note that due to cantilever drift, especially in the horizontal direction, the alignment may immediately drift away from the optimum. Nonetheless, avoid adjusting the screws again.
   4. Select "Move back from the alignment station."
   5. Refocus the camera on the cantilever and move the red cross to the tip's position by clicking in the camera window. This will later specify the point of contact with the sample. Position the cross above the metal plate where measurements will be performed, as the background affects the visible position of the tip.
   6. Note the vertical and horizontal drift in the logbook.

f. Cantilever tuning
   An in-depth discussion of the torsional resonances can be found in the theoretical background Sect. 2.2, in the description of the TR mode Sect. 3.1.4 and the discussion of the results Sect. 4.2.

   1. Select "Cantilever Tune" to find the torsional resonance modes without using the "AutoTune" tool.

2. Set the lock-in amplifier bandwidth ("Tr Lock-in BW") to 0.211 kHz (the lowest possible value) to reduce noise in the resonance curves.
3. Set the "TR drive amplitude" to 20 mV.
4. Zoom out to view the full spectrum. For the cantilever used in this work, the torsional resonance is typically found at 600 - 800 kHz or $\sim$ 1100 kHz.
5. Set "Coupling Check" to "on."
   The previously displayed lateral amplitude (C-D) will be replaced by the vertical amplitude (A-B), while the cantilever continues to be driven in the same manner. A fully torsional or lateral bending mode should not show any signal in the vertical deflection channel, indicating that vertical bending (tapping) and torsional resonances do not overlap. If there is an overlap or coupling, a larger peak will appear on or near the previously displayed peak. If this happens, either choose another torsional mode or replace the cantilever. This issue usually does not occur for the types of cantilevers used, (see Fig. 4.1).
6. Turn off "Coupling Check" and reduce the displayed frequency range to around 40 kHz.
7. Click on "More" and select "Balance Tune" to ensure both torsional piezos are driven equally.
8. Click on "Center Peak" and "Zero Phase" to center the peak and shift the phase so that the corresponding peak has a "zero phase."
9. Exit "Cantilever Tune."
10. Note any drift in the logbook.

g. Navigate to the sample
   1. Note the drift in the logbook, this is the last time vertical drift provides a useful measure and is needed to engage with a correct setpoint.

h. Check parameters

   These are the parameters used for later engaging and should mostly already be set correctly. Copy the settings in Fig. A.4 (a) but you might only need to adjust the following: "Scan Size" (10 nm), "Scan rate" (4-6 Hz), "TR Drive Amplitude" (8 mV), "TR Lock-in BW" (2 kHz), "Z-limit" ($4 - 6\,\mu$m).

   Select the appropriate "TR Deflection Setpoint" to ensure that the engagement does not exert excessive loading force (typically around 50 nN). The setpoint corresponding to a certain force is calculated using the formula:

$$\frac{\text{force}}{\text{spring constant} \times \text{deflection sensitivity}} + \text{vertical deflection}$$

   With the vertical deflection from the logbook, previously noted. However, accurately determining the spring constant and deflection sensitivity, as discussed in Sect. 4.1, remains challenging but may not needed for just determining θ. Our experience shows a setpoint of 100 mV (+vertical deflection) is reasonable.

i. Press "Engage", which is an autonomous process with the already set parameters.

(a)

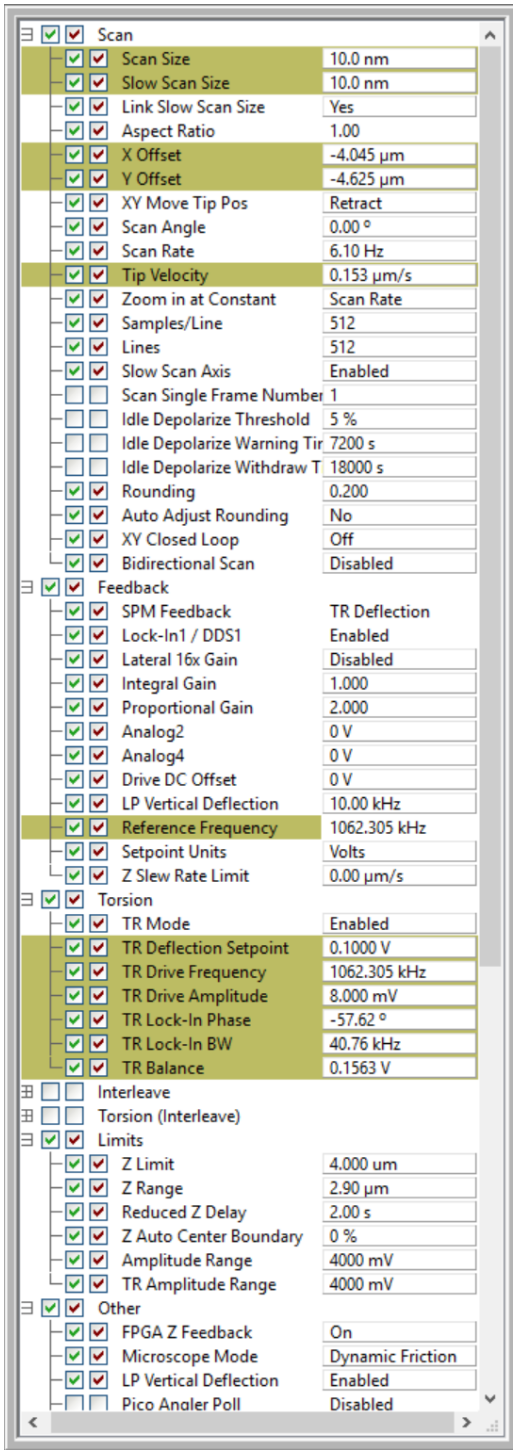

(b)

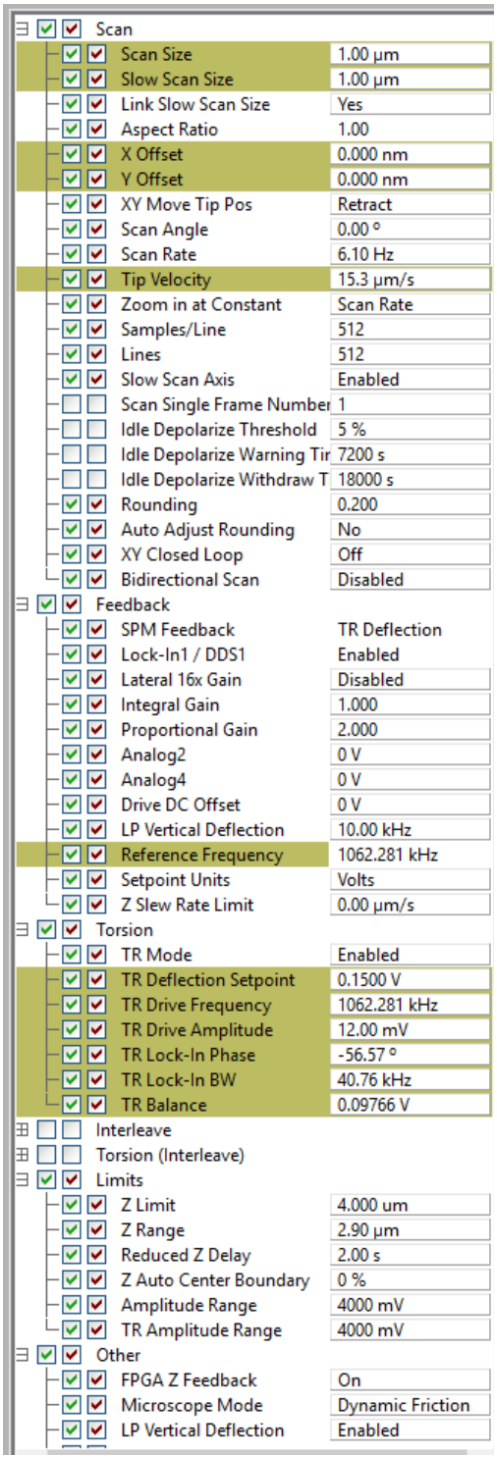

Figure A.4: *(a) Engage setting and (b) exemplaric scan setting.*

Scanning

After successful contact was made the AFM starts scanning. The displayed channels should be "Height Sensor", "TR Deflection Error", "TR Amplitude", and "TR Phase", with the moiré superpotential being visible in amplitude and phase images.

According to our empirical findings (see Sect. 4.3). The most effective parameters are Scan rate" (6 - 16 Hz), "TR Drive Amplitude" (8 - 24 mV), "TR Deflection Setpoint" (0.05 - 0.2 V), "TR Lock-in BW" (2 - 100 kHz). Exemplary scan settings are provided in Fig. A.4 (b).

a. Increase scan area to about $4 - 8\,\mu m$ to move over the sample and find a region of interest (R.O.I). The edges of graphene and domain walls, small folds or cracks will be visible. If the image looks noisy, perform steps d. and e. at this point already (and later again). Larger scan areas generally need a smaller scan rate, for an in-depth discussion of choosing the right parameters, see Sect. 4.3.5.

b. Reduce scan area to about $1 - 2\,\mu m$ for large moirés and 100 nm for the ones near MATBG, after R.O.I was found.

c. Determination of "Contact + 0 nN" setpoint

   Since we are not interested in determining the exact applied force, this step does not require the accuracy as described in the supplementary material of Ref. [35]. However, it still gives information on how much force is roughly applied to not exceed a critical value, at which the tip and sample may be damaged.

   Here we note the "Last point of contact", "Flying condition" and "Snapback" in the logbook. The "Last point of contact" will be treated equally to "Contact + 0nN", thus serving as a reference point for any later setpoint increases.

   1. Lower the deflection setpoint in steps of 20mV while observing the voltage and bar of the Z-piezo and output channels.
   2. When observing a slight drop in the voltage of the deflection Z-piezo, choose a smaller step size. At some point, the voltage suddenly drops, the bar turns red and the channels show no signal. The amplitude of cantilever motion (visible at the bottom left window) increases. Note this deflection setpoint as "Flying condition".
   3. Increase the setpoint again and lower it while carefully looking at the channels. Right before the cantilever loses contact, this deflection is noted as "Last point of contact".
   4. Increase the deflection setpoint to roughly 60 mV with respect to "Contact + 0 nN".

d. "Generic Sweep"

   From the resonance of a free cantilever, the torsional resonant frequency typically increases, while the amplitude decreases due to tip-sample interactions. These frequency and amplitude shifts become more pronounced with higher loading forces. Using "Generic Sweep," adjust the drive frequency so that the cantilever is driven

at resonance. This adjustment is critical for obtaining a moiré image and must be performed each time there is a significant change in the force or a different R.O.I is selected.

1. Click on “Generic Sweep” and set “0 nm” in the window that pops up.
2. Set “TR Lock-in BW” to 0.211 Hz and “TR Drive Amplitude” to 20 mV.
   Note: It may help to already enable “Lateral 16x gain”, which amplifies the measured amplitude by 16 for better visibility of small changes and therefore also increases the resonance peak.
3. Click on “Center peak” to center it and “Zero phase” or select the center manually.
4. Return by clicking “Exit”.

e. Adjust scan settings After completing steps c. and d., the moiré pattern should be visible. Fine-tune the parameters by systematically adjusting the most impactful ones (as mentioned above). These adjustments are optimized for our sample (device number 1) and a relatively large moiré periodicity but might vary only slightly for most tBG on a soft polymer stamp.

1. Start saving image files with the correct filename to the chosen directory in the top right corner. The software does not save every single image continuously, thus a regular check is important, to not lose any data.
2. Enable ”Lateral 16x gain”
3. Increase the “TR Lock-in BW” to 60-100 kHz
4. Set the Scan rate” to 8kHz, it can be later adjusted between 6-16Hz, depending on the size of the scan area.
5. Increase “TR Deflection Setpoint” in steps of 10-20 mV until optimal contrast is obtained.
6. “TR Drive Amplitude” increase to 8-12 Hz, 16-24 Hz may help as well.
7. Take notes of obtained images and parameters in the logbook.

f. End measuring session

1. Click “Withdraw” to retract from the sample surface and stop the measuring process.
2. Return to “Navigating” to raise the scan head and move the plate.

Appendix B

Determining the twist angle in Gwyddion

In the post-processing of AFM images of twisted bilayer graphene, several filtering techniques are employed to enhance the quality and accuracy of the data analysis. The buttons of the filters within the software are color-coded in Fig. B.1 (a), for easy reproducibility. Initially, "row alignment using various methods" is performed, such as fitting a polynomial of a certain degree, to correct any misalignments in the image rows. This alignment ensures that the image data accurately reflects the sample's surface topography by eliminating any systematic offsets. Next, "remove polynomial background" is applied

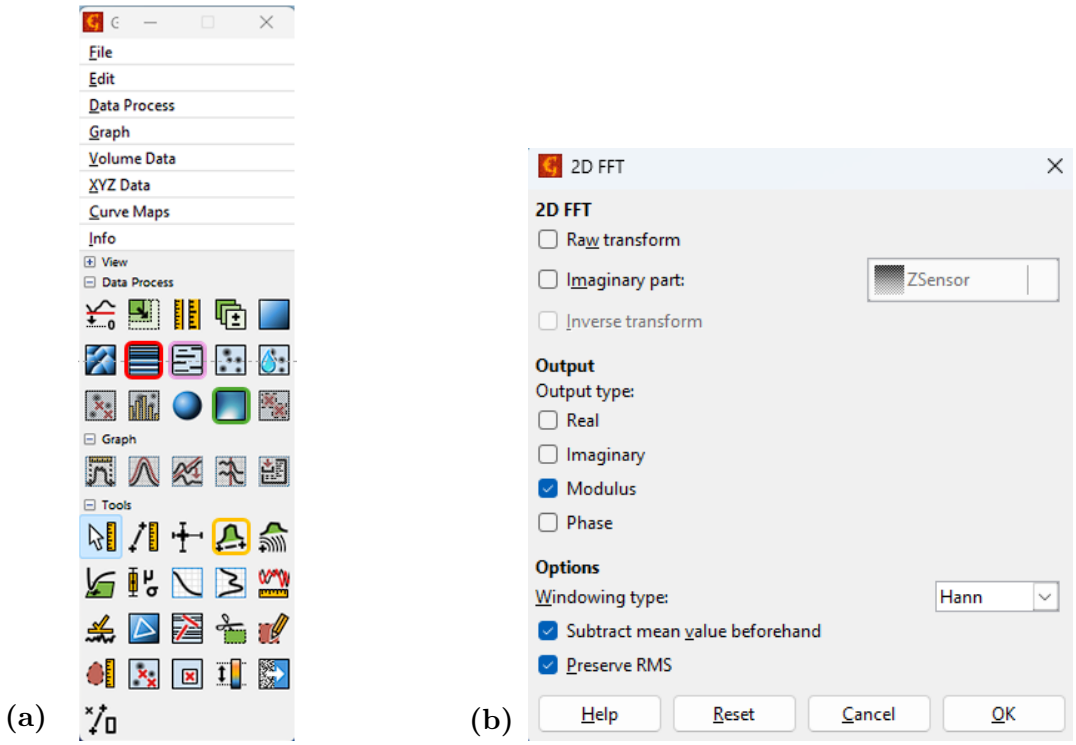

(a) (b)

Figure B.1: *(a) Screenshot of the program Gwyddion. Employed filters and other methods are color-coded by a square outline: "Row alignment using various methods" (red), "Remove polynomial background" (green), "Correct horizontal scars" (pink), "Extract line profile" (orange). (b) Screenshot of 2D FFT window and chosen output and window function settings*

to the data to correct for any large-scale height variations. This step involves fitting a polynomial surface to the background and subtracting it, thereby enhancing the visibility of smaller features and periodic structures, such as the moiré pattern. Additionally, "correct horizontal scars" is employed to address any scanning artifacts or lines that may appear in the image due to imperfections in the scanning process. Although this correction is not considered crucial, it helps improve the overall visual quality. Together, these filtering techniques refine the AFM data, ensuring that subsequent analyses (e.g. 2D FFT) accurately capture the properties of the tbG.

After saving the processed image, proceed by applying the 2D FFT, which's algorithm was already described in Chap. 3.3.2. By selecting "Data Process" → "Integral transform" → "2D FFT", the FFT window, shown in Fig. B.1 (b) opens up . The 'Modulus' output was selected to capture the magnitude of the Fourier coefficients, and the 'Hann' window function was employed to reduce spectral leakage. Additionally, the options 'Subtract mean value beforehand' and 'Preserve RMS' were enabled to ensure data integrity by removing the mean and maintaining the root mean square amplitude.

In theory, six hexagonally arranged peaks should be visible in the Fourier space image, representing the characteristic features of the moiré pattern. Using the 'Extract line profile' tool (see Fig. B.1 (a), three line profiles were extracted to facilitate analysis. The distance between the two main peaks of each line profile was measured, which corresponds to the predominant periodicity of the moiré lattice (denoted as distance x) and can be directly used in Equation (3.2) to calculate the twist angle. When the moiré pattern exhibits minimal strain, averaging the twist angle across all three line profiles provides a comprehensive measure, reflecting the angle in all three directions of the hexagonal lattice. Furthermore, the FFT inherently averages the twist angle over the entire scan area, enhancing the reliability of the measurement. If the image exhibits regions with varying twist angles (e.g. Fig. 4.10 (e) and (f)), it is advisable to crop these regions before processing them with FFT.

Appendix C

The 01R2 cantilever and first images

The first cantilever we used was effective because it shared similarities with the one used by Pendharkar. We demonstrated its capabilities in, seen in Fig. C.1 (a), covering a large scan area, (b) achieving high contrast on medium-length scales, and (d) delivering high resolution in small areas. The latter closely resembles the zoomed-in results obtained with the NSC18 (see Fig. 4.4 (f)), even revealing the inhomogeneous structure of the AA domains, which could be attributed to gradual and non-uniform changes in stacking configurations. Fig. C.1 (c) shows relatively poor contrast but is included to emphasize once again that accurate twist angle calculations can still be achieved. Despite the low contrast, the FFT could filter the main periodicity, yielding a reasonable result of approximately $\theta \approx 0.08^\circ$ compared to other images.

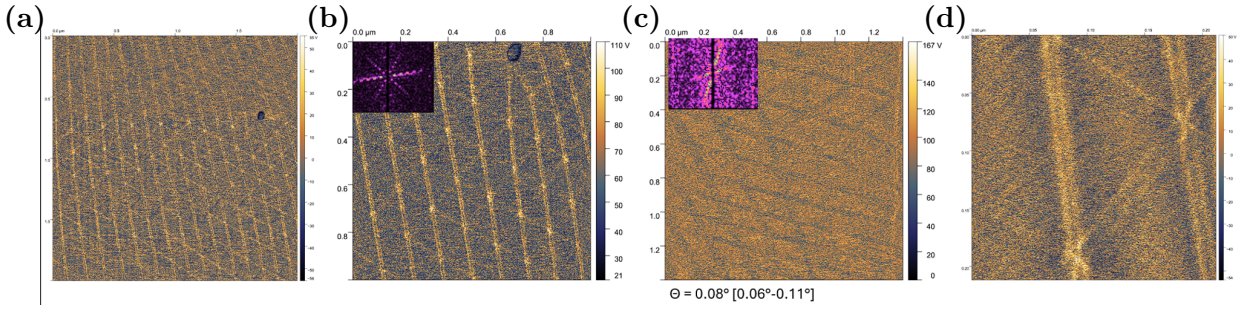

Figure C.1: *The first cantilever (01R2) used, also conductive coated and similar to the one in Pendharkar's study [15], demonstrated effective performance across different scales: (a) covering a large scan area, (b) achieving high contrast on medium-length scales, and (d) delivering high resolution in small areas, revealing the inhomogeneous structure of AA domains. In contrast, (c) shows relatively poor contrast, yet still allows for accurate twist angle calculations, with 2D-FFT yielding a reasonable $\theta \approx 0.08^\circ$. Images acquired with 01R2, with parameters in (c) [defl.: 0.16 V, scan: 8 Hz, drive: 4 mV, bw: 100 kHz].*

Bibliography

[1] Gordon E Moore. "Cramming more components onto integrated circuits". In: *Proceedings of the IEEE* 86.1 (1998), pp. 82–85.

[2] Thomas N Theis and H-S Philip Wong. "The end of moore's law: A new beginning for information technology". In: *Computing in science & engineering* 19.2 (2017), pp. 41–50.

[3] Kostya S Novoselov et al. "Electric field effect in atomically thin carbon films". In: *science* 306.5696 (2004), pp. 666–669.

[4] Darsith Jayachandran et al. "Three-dimensional integration of two-dimensional field-effect transistors". In: *Nature* 625.7994 (2024), pp. 276–281.

[5] Y Ravi Kumar et al. "Graphene quantum dot based materials for sensing, bio-imaging and energy storage applications: a review". In: *RSC advances* 10.40 (2020), pp. 23861–23898.

[6] Ababay Ketema Worku and Delele Worku Ayele. "Recent advances of graphene-based materials for emerging technologies". In: *Results in Chemistry* 5 (2023), p. 100971.

[7] Andre K Geim and Irina V Grigorieva. "Van der Waals heterostructures". In: *Nature* 499.7459 (2013), pp. 419–425.

[8] Yuan Cao et al. "Unconventional superconductivity in magic-angle graphene superlattices". In: *Nature* 556.7699 (Apr. 2018). Publisher: Nature Publishing Group, pp. 43–50. ISSN: 1476-4687. DOI: 10.1038/nature26160. URL: https://www.nature.com/articles/nature26160 (visited on 07/23/2024).

[9] Yuan Cao et al. "Correlated insulator behaviour at half-filling in magic-angle graphene superlattices". In: *Nature* 556.7699 (2018), pp. 80–84.

[10] Kevin P Nuckolls et al. "Strongly correlated Chern insulators in magic-angle twisted bilayer graphene". In: *Nature* 588.7839 (2020), pp. 610–615.

[11] Yuan Cao et al. "Unconventional superconductivity in magic-angle graphene superlattices". In: *Nature* 556.7699 (2018), pp. 43–50.

[12] Rafi Bistritzer and Allan H MacDonald. "Moiré bands in twisted double-layer graphene". In: *Proceedings of the National Academy of Sciences* 108.30 (2011), pp. 12233–12237.

[13] Chun Ning Lau et al. “Reproducibility in the fabrication and physics of moiré materials”. In: *Nature* 602.7895 (2022), pp. 41–50.

[14] J Díez-Mérida et al. “High-yield fabrication of bubble-free magic-angle twisted bilayer graphene devices with high twist-angle homogeneity”. In: ().

[15] Mihir Pendharkar et al. “Torsional force microscopy of van der Waals moirés and atomic lattices”. In: *Proceedings of the National Academy of Sciences* 121.10 (Mar. 5, 2024), e2314083121. ISSN: 0027-8424, 1091-6490. DOI: 10.1073/pnas.2314083121. URL: https://pnas.org/doi/10.1073/pnas.2314083121 (visited on 06/07/2024).

[16] Cheng Hu et al. “In-situ twistable bilayer graphene”. In: *Scientific Reports* 12 (Jan. 7, 2022). DOI: 10.1038/s41598-021-04030-z.

[17] Leo J. McGilly et al. “Visualization of moiré superlattices”. In: (July 2020). URL: https://www.nature.com/articles/s41565-020-0708-3 (visited on 05/28/2024).

[18] Junxi Yu et al. “Imaging Graphene Moiré Superlattices via Scanning Kelvin Probe Microscopy”. In: *Nano Letters* 21.7 (Apr. 14, 2021). Publisher: American Chemical Society, pp. 3280–3286. ISSN: 1530-6984. DOI: 10.1021/acs.nanolett.1c00609. URL: https://doi.org/10.1021/acs.nanolett.1c00609 (visited on 05/28/2024).

[19] Roop Kumar Mech et al. *Versatile polymer method to dry-flip two-dimensional moir\'e hetero structures for nanoscale surface characterization*. June 4, 2024. arXiv: 2406.02819[cond-mat]. URL: http://arxiv.org/abs/2406.02819 (visited on 06/10/2024).

[20] N David Mermin. “Crystalline order in two dimensions”. In: *Physical review* 176.1 (1968), p. 250.

[21] Sumio Iijima and Toshinari Ichihashi. “Single-shell carbon nanotubes of 1-nm diameter”. In: *nature* 363.6430 (1993), pp. 603–605.

[22] John A Venables. “Atomic processes in crystal growth”. In: *Surface Science* 299 (1994), pp. 798–817.

[23] François Varchon et al. “Electronic structure of epitaxial graphene layers on SiC: effect of the substrate”. In: *Physical review letters* 99.12 (2007), p. 126805.

[24] Luis EF Foa Torres, Stephan Roche, and Jean-Christophe Charlier. *Introduction to graphene-based nanomaterials: from electronic structure to quantum transport*. Cambridge university press, 2014.

[25] Philip Richard Wallace. “The band theory of graphite”. In: *Physical review* 71.9 (1947), p. 622.

[26] Wikipedia. *Graphene - sigma and pi bonds*. 2024. URL: https://en.wikipedia.org/wiki/Graphene (visited on 08/13/2024).

[27] Antonio H Castro Neto et al. “The electronic properties of graphene”. In: *Reviews of modern physics* 81.1 (2009), pp. 109–162.

[28] Andre K Geim and Konstantin S Novoselov. “The rise of graphene”. In: *Nature materials* 6.3 (2007), pp. 183–191.

[29] Felix Bloch. "Über die quantenmechanik der elektronen in kristallgittern". In: *Zeitschrift für physik* 52.7 (1929), pp. 555–600.

[30] Stephanie Reich et al. "Tight-binding description of graphene". In: *Physical Review B* 66.3 (2002), p. 035412.

[31] JMB Lopes dos Santos, NMR Peres, and AH Castro Neto. "Graphene bilayer with a twist: electronic structure". In: *Physical review letters* 99.25 (2007), p. 256802.

[32] João Fernandes da Silva, Lucas Allende Dias do Nascimento, and Simone dos Santos Hoefel. "Free vibration analysis of Euler-Bernoulli beams under non-classical boundary conditions". In: *IX Congresso Nacional de Engenharia Mecânica CONEM2016, Fortaleza-CE, Brasil*. 2016.

[33] © Bruker Corporation. *TRmode*. 2011. URL: https://nanoqam.ca/wiki/lib/exe/fetch.php?media=support_note_trmode_v7-j_013-416-000_.pdf (visited on 08/14/2024).

[34] Saima A Sumaiya, Jun Liu, and Mehmet Z Baykara. "True atomic-resolution surface imaging and manipulation under ambient conditions via conductive atomic force microscopy". In: *ACS nano* 16.12 (2022), pp. 20086–20093.

[35] Mihir Pendharkar et al. "Supporting information for: Torsional force microscopy of van der Waals moirés and atomic lattices". In: *Proceedings of the National Academy of Sciences* 121.10 (Mar. 5, 2024), e2314083121. ISSN: 0027-8424, 1091-6490. DOI: 10.1073/pnas.2314083121. URL: https://www.pnas.org/doi/10.1073/pnas.2314083121#supplementary-materials (visited on 07/12/2024).

[36] Gerd Binnig et al. "Surface studies by scanning tunneling microscopy". In: *Physical review letters* 49.1 (1982), p. 57.

[37] Gerd Binnig, Calvin F Quate, and Ch Gerber. "Atomic force microscope". In: *Physical review letters* 56.9 (1986), p. 930.

[38] Hang Zhang et al. "Atomic force microscopy for two-dimensional materials: A tutorial review". In: *Optics Communications*. Optoelectronics and Photonics Based on Two-dimensional Materials 406 (Jan. 1, 2018), pp. 3–17. ISSN: 0030-4018. DOI: 10.1016/j.optcom.2017.05.015. URL: https://www.sciencedirect.com/science/article/pii/S0030401817303887 (visited on 05/28/2024).

[39] Nader Jalili and Karthik Laxminarayana. "A review of atomic force microscopy imaging systems: application to molecular metrology and biological sciences". In: *Mechatronics* 14.8 (2004), pp. 907–945.

[40] Thilo Glatzel, Urs Gysin, and Ernst Meyer. "Kelvin probe force microscopy for material characterization". In: *Microscopy* 71.Supplement_1 (2022), pp. i165–i173.

[41] Yibo Wang. "Characterization and electronic properties of moiré superlattices in van der Waals heterostructures". PhD thesis. University of Manchester, 2019. URL: https://research.manchester.ac.uk/files/170763734/FULL_TEXT.PDF.

[42] © Bruker Corporation Bede Pittenger. *Application Note AN158, Torsional resonance modes*. on Bruker.com. Accessed: 2023-08-14. 2024. URL: https://www.bruker.com/en/products-and-solutions/microscopes/materials-afm/resource-library/an-158-torsional-resonance-modes.html#ID_access-form.

[43] P. J. Zomer et al. "Fast pick up technique for high quality heterostructures of bilayer graphene and hexagonal boron nitride". In: *Applied Physics Letters* 105.1 (July 7, 2014), p. 013101. ISSN: 0003-6951, 1077-3118. DOI: 10.1063/1.4886096. URL: https://pubs.aip.org/apl/article/105/1/013101/596305/Fast-pick-up-technique-for-high-quality (visited on 06/03/2024).

[44] Andres Castellanos-Gomez et al. "Deterministic transfer of two-dimensional materials by all-dry viscoelastic stamping". In: *2D Materials* 1.1 (2014), p. 011002.

[45] Yuan Huang et al. "Reliable Exfoliation of Large-Area High-Quality Flakes of Graphene and Other Two-Dimensional Materials". In: *ACS Nano* 9.11 (Nov. 24, 2015). Publisher: American Chemical Society, pp. 10612–10620. ISSN: 1936-0851. DOI: 10.1021/acsnano.5b04258. URL: https://doi.org/10.1021/acsnano.5b04258 (visited on 06/03/2024).

[46] Amol Nimbalkar and Hyunmin Kim. "Opportunities and challenges in twisted bilayer graphene: a review". In: *Nano-Micro Letters* 12 (2020), pp. 1–20.

[47] P. Blake et al. "Making graphene visible". In: *Applied Physics Letters* 91.6 (Aug. 6, 2007), p. 063124. ISSN: 0003-6951, 1077-3118. DOI: 10.1063/1.2768624. URL: https://pubs.aip.org/apl/article/91/6/063124/1023191/Making-graphene-visible (visited on 06/03/2024).

[48] Karen Reinhardt and Werner Kern. *Handbook of silicon wafer cleaning technology*. William Andrew, 2018.

[49] Christophe Cardinaud, Marie-Claude Peignon, and Pierre-Yves Tessier. "Plasma etching: principles, mechanisms, application to micro-and nano-technologies". In: *Applied Surface Science* 164.1-4 (2000), pp. 72–83.

[50] ZH Ni et al. "Graphene thickness determination using reflection and contrast spectroscopy". In: *Nano letters* 7.9 (2007), pp. 2758–2763.

[51] Rebeca Ribeiro-Palau et al. "Twistable electronics with dynamically rotatable heterostructures". In: *Science* 361.6403 (2018), pp. 690–693.

[52] Ji Qingxiang et al. "Interlayer torsional sliding and strain localization in bilayer graphene". In: *Proceedings of the Royal Society A: Mathematical, Physical and Engineering Sciences* 479 (Apr. 19, 2023). DOI: 10.1098/rspa.2022.0833.

[53] Matthew Yankowitz et al. "Emergence of superlattice Dirac points in graphene on hexagonal boron nitride". In: *Nature Physics* 8.5 (May 2012). Publisher: Nature Publishing Group, pp. 382–386. ISSN: 1745-2481. DOI: 10.1038/nphys2272. URL: https://www.nature.com/articles/nphys2272 (visited on 07/22/2024).

[54] Tjerk Benschop et al. "Measuring local moiré lattice heterogeneity of twisted bilayer graphene". In: *Physical Review Research* 3 (Feb. 16, 2021). DOI: 10.1103/PhysRevResearch.3.013153.

[55] Matteo Frigo and Steven G Johnson. "The design and implementation of FFTW3". In: *Proceedings of the IEEE* 93.2 (2005), pp. 216–231.

[56] Petr Klapetek, David Nečas, and Christopher Anderson. *Gwyddion User Guide*. Copyright ©2004–2007, 2009–2023. 2004–2023. URL: `http://gwyddion.net/documentation/user-guide-en/fourier-transform.html` (visited on 08/03/2024).

[57] Christopher P Green and John E Sader. "Torsional frequency response of cantilever beams immersed in viscous fluids with applications to the atomic force microscope". In: *Journal of applied physics* 92.10 (2002), pp. 6262–6274.

[58] © Bruker Corporation. *NanoScope V Controller Manual*. 2011. URL: `https://nanoqam.ca/wiki/lib/exe/fetch.php?media=nanoscope_v_controller_manual-f_004-992-000_.pdf` (visited on 08/14/2024).

[59] Aviram Uri et al. "Mapping the twist-angle disorder and Landau levels in magic-angle graphene". In: *Nature* 581.7806 (2020), pp. 47–52.

Declaration of authorship

I hereby declare that the thesis submitted is my own unaided work. All direct or indirect sources used are acknowledged as references. I am aware that the thesis in digital form can be examined for the use of unauthorized aid and in order to determine whether the report as a whole or parts incorporated in it may be deemed as plagiarism. For the comparison of my work with existing sources I agree that it shall be entered in a database where it shall also remain after examination, to enable comparison with future theses submitted. Further rights of reproduction and usage, however, are not granted here. This paper was not previously presented to another examination board and has not been published.

Munich, 02.09.2024

Quentin Fuchs